Performance Analysis of IMD High-Resolution Gridded Rainfall (0.25° × 0.25°) and Satellite Estimates for Detecting Cloudburst Events over the Northwest Himalayas

PRAVAT JENA, SOURABH GARG, AND SARITA AZAD

School of Basic Sciences, Indian Institute of Technology Mandi, Himachal Pradesh, India

(Manuscript received 19 December 2019, in final form 23 April 2020)

ABSTRACT

The presence of a sparse rain gauge network in complex terrain like the Himalayas has encouraged the present study for the concerned evaluation of Indian Meteorological Department (IMD) ground-based gridded rainfall data for highly prevalent events like cloudbursts over the northwest Himalayas (NWH). To facilitate the abovementioned task, we intend to evaluate the performance of these observations at 0.25° × 0.25° (latitude–longitude) resolution against a predefined threshold (i.e., 99.99th percentile), thereby initially comprehending the success of IMD data in capturing the cloudburst events reported in media during 2014–16. Further, seven high-resolution satellite products, namely, CMORPH V0.x, PERSIANN-CDR, TMPA 3B42RT V7, IMERG V06B, *INSAT-3D* multispectral rainfall (IMR), CHIRPS V.2, and PERSIANN-CCS are evaluated against the IMD dataset. The following are our main results. 1) Six out of 18 cloudburst events are detected using IMD gridded data. 2) The contingency statistics at the 99.99th percentile reveal that the probability of detection (POD) of TMPA varies from 19.4% to 53.9% over the geographical stretch of NWH, followed by PERSIANN-CDR (18.6%–48.4%) and IMERG (4.9%–17.8%). 3) A new metric proposed as improved POD (IPOD) has been developed in this work, which takes into account the temporal lag that exists between observed and satellite estimates during an event period. Results show that for an event analysis IPOD provides a better comparison. The IPOD for TMPA is 32.8%–74.4%, followed by PERSIANN-CDR (34.4%–69.11%) and IMERG (15.3%–39.0%). 4) The conclusion stands as precipitation estimates obtained from CHIRPS are most suitable for monitoring cloudburst events over NWH with IPOD of 60.5%–78.6%.

1. Introduction

The Himalayan ranges, spanning an area of 2400 km^2 on the Asian continent, play a vital role in governing weather patterns and controlling the climate over northern India. On average, the western Himalayas get around 60 in. (1530 mm) of rainfall annually, while the eastern Himalayas receive 120 in. (3050 mm). Apart from this amount of rain received, the region is exposed to extreme weather conditions that have witnessed an increase in frequency from 1910 to 2000 (Sen Roy and Balling 2004). The excessive rainfall events like cloudbursts often occur at mesoscale (2–20 km) (Orlanski 1975) and are generally defined as a sudden massive rainfall deluge causing secondary events like flash floods, landslides, dam breaks, etc. (Dimri and Dash 2012; Das et al. 2006). Generally, such events occur during the monsoon season and constitute the dominant natural hazards in the region. Different rainfall intensities for the identification of cloudburst events have been reported in the literature (Guhathakurta et al. 2011; Nandargi and Dhar 2012; Goswami et al. 2006; Rajeevan et al. 2008). For example, for the study of the extreme rainfall events, Goswami and Ramesh (2008) used 250 mm day^{-1} as a threshold, while Nandargi and Dhar (2012) have considered rainfall intensity of more than 200 mm day^{-1} as heavy rainfall over the northwest Himalayas (NWH). The rainfall intensities associated with high quantiles of precipitation distribution above the 99.99th percentile are considered as a threshold to define cloudburst events (Bharti et al. 2016). These events destroy life and property, for example, the remarkably intense monsoon rainfalls in Kedarnath (Uttarakhand) with rainfall intensities above 200 mm day^{-1} during 15–18 June 2013 (Parida et al. 2017) resulted in more than 6000 casualties. Almost 50 million people in five countries (Nepal, India, Bhutan, China, and Pakistan) live in the Himalayas. Cloudburst prediction is crucial for the region, but the current prediction models are not accurate (Das et al. 2006;

Corresponding author: Sarita Azad, sarita@iitmandi.ac.in

DOI: 10.1175/JHM-D-19-0287.1

Chevuturi et al. 2015). There is a severe challenge in calibrating these models because of an insufficient number of observational stations in complex terrain (Singh and Mal 2014). Since the Indian Meteorological Department (IMD) gridded dataset is used for most of the validation studies, in this paper we posit that these observed data should be evaluated because of the two reasons. First, due to the Himalayas's complex terrain, IMD has a sparse network (Parida et al. 2017) in the region and only unequally scattered point stations are available. IMD gridded data of resolution 0.25° × 0.25° are derived through interpolation of stations available up to 1.5°, with the weight assigned to each station which decreases as the distance increases from the interpolation point to the station (Pai et al. 2014). The resultant interpolated values in complex terrains are likely to have more errors due to more dispersed station density (Roy Bhowmik and Das 2007; Mishra 2013; Hofstra et al. 2010). Therefore, it becomes essential to evaluate this dataset as extreme events are more sensitive to interpolation errors (Herrera et al. 2012). To the best of our knowledge, IMD gridded data had not been evaluated for cloudburst events. Second, IMD gridded data are the only available source of the observed data for monitoring and model evaluation, owing to the frequent occurrence of cloudbursts in ungauged locations, and it subsequently brings forth the importance of the evaluation of gridded data.

Further, satellite estimates are currently being used as an alternate source of data for monitoring and validation purposes since they are available at high spatiotemporal scales as models (Dinku et al. 2014). Some of these products are, Climate Prediction Center Morphing technique (CMORPH), Precipitation Estimation from Remotely Sensed Information Using Artificial Neural Networks–Climate Data Record (PERSIANN-CDR), Tropical Rainfall Measuring Mission (TRMM) Multisatellite Precipitation Analysis (TMPA), Integrated Multisatellite Retrievals for GPM (IMERG), *Indian National Satellite-3D* (*INSAT-3D*) Multispectral Rainfall (IMR), Climate Hazards Group Infrared Precipitation with Station Data (CHIRPS), and PERSIANN–Cloud Classification System (PERSIANN-CCS).

Across the globe, intercomparison and validation of these products with ground observations have been proved as a significant point of the study (Dinku et al. 2007; Feidas 2010; Qin et al. 2014; Hessels 2015; Beck et al. 2011). For the Indian subcontinent, TRMM estimates have been mainly utilized for regional studies (Nair et al. 2009; Rahman et al. 2009; Mitra et al. 2013; Prakash et al. 2014, 2015, 2018). Recently conducted studies over the Himalayan region illustrate the improved sign of rainfall in conjunction with the latest version of TMPA-3B42 version 7 (V7) (Bharti and Singh 2015; Bharti et al. 2016; Parida et al. 2017; Dahiya et al. 2020). A study carried by Parida et al. (2017) reported that TMPA-3B42V7 estimates are more accurate compared to other satellite products such as CMORPH and Global Satellite Mapping of Precipitation (GSMaP) for cloudburst event over Uttarakhand during June 2013.

Recently, IMERG product has provided enhanced spatiotemporal resolution data and assessed for heavy rainfall detection against gauge-based observations over India (Prakash et al. 2018; Beria et al. 2017). It has been reported to show improvement over TMPA-3B42 V7 and *INSAT-3D* (Singh et al. 2018; Prakash et al. 2018). Even though overall errors in IMERG were reduced, it still has large uncertainty over orographic regions (e.g., Houze 2012; Derin and Yilmaz 2014; Mei et al. 2014; Prakash et al. 2014), and it is reported to have high-magnitude biases for the rain intensities greater than 100 mm day^{-1} over China and different regions in India (Chen et al. 2018; Prakash et al. 2018). Further, Rao et al. (2020) and Mitra et al. (2018) investigated the performance of *INSAT-3D* over the Indian region. They suggested that this dataset has the potential to be used for weather forecasting and nowcasting applications. However, it underestimates heavy rainfall and is unable to detect orographic rain.

On finescale satellite estimates, namely, CHIRPS, a study conducted by Katsanos et al. (2016) over the Mediterranean basin illustrated its relationship with gauge-based rainfall estimates and reported a moderate (<0.5) correlation exhibit between the two datasets. Further, a study carried by Aadhar and Mishra (2017) found that the CHIRPS underestimates the rainfall over complex terrain like Western Ghats and Himalayas. In turn, it suggests that the CHIRPS can detect high percentile rainfall over plain regions, whereas it fails to recognize in the hilly and mountainous area. Further, a study carried out by Hong et al. (2007) illustrated the use of finescale PERSIANN-CCS in capturing spatial distribution, the timing of diurnal convective rainfall, and elevation-dependent biases. It is found to underestimates the daily precipitation at high elevations and overestimates it at low altitudes.

To summarize, several satellites have been successful in facilitating the representation of the rainfall over plains (Rahman et al. 2009), whereas for their mountainous counterparts they fail and incur significant errors (Kumar et al. 2016; Prakash et al. 2018; Hong et al. 2007). This draws our immediate attention and focuses on the evaluation of multisatellite products available at high resolution to monitor and predict extreme rainfall events over the mountainous terrain of NWH.

Also, from the literature, it is noticed that IMD observed data of 0.25° × 0.25° resolution has not been

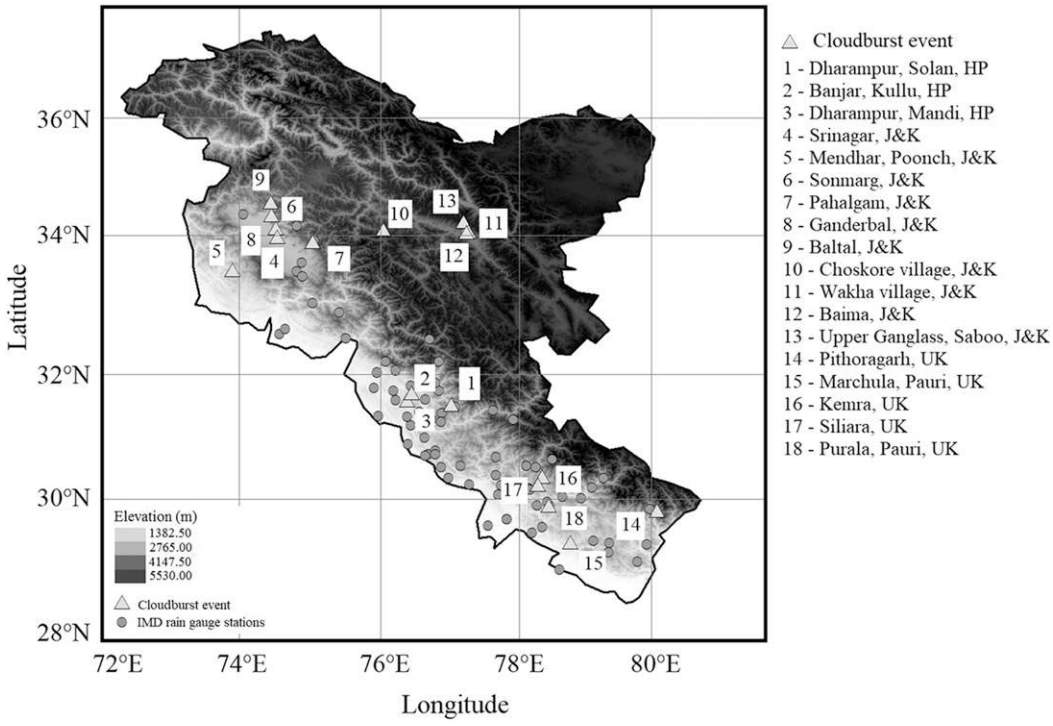

FIG. 1. The locations of 18 cloudburst events occurred during 2014–16 over NWH along with 77 functional stations of IMD.

evaluated for highly prevalent events like cloudbursts over NWH. Therefore, we intend to evaluate the performance of these observations against a predefined threshold (which is generally perceived as 99.99th percentile), thereby initially comprehending the success of IMD data in capturing the cloudburst events. Further, seven satellite-retrieved precipitation products, namely, CMORPH V0.x (0.25° × 0.25°), PERSIANN-CDR (0.25° × 0.25°), TMPA 3B42RT V7 (0.25° × 0.25°), *INSAT-3D* IMR (0.1° × 0.1°), IMERG V06B (0.1° × 0.1°) are evaluated against IMD gridded dataset of 0.25° × 0.25° resolution. And, two finescale resolution satellite products, namely, CHIRPS V.2 (0.05° × 0.05°), and PERSIANN-CCS (0.04° × 0.04°) are evaluated against gauge station data as IMD gridded data of resolution 0.25° × 0.25° will be too coarse to compare with finescale estimates.

2. Study region, data, and methodology

a. Study region

The present study focuses on the area of NWH that includes three hilly states of India, namely, Uttarakhand (U.K.), Himachal Pradesh (HP), and Jammu and Kashmir (J&K). It spans from 28.5° to 37°N in latitude and from 72° to 81°E in longitude (Fig. 1). The study area includes a region with complex orography influenced by the Hindu Raj mountain range to the north, the Kunlun mountain range toward the northeast, and Garhwal Himalayas in the lower belt of NWH. This region is chosen for the study because of the increasing instances of extreme rainfall events in recent times (Dimri et al. 2017).

b. Data

1) OBSERVED DATA

The data utilized in the present study include IMD observations of 0.25° × 0.25° latitude–longitude resolution, which are taken as ground truth (http://www.tropmet.res.in).

This dataset has been developed using rainfall observations from 6955 gauge stations over India, whereas there are approximately 77 stations over NWH. The inverse distance weighted interpolation (IDW) method developed by Shepard (1968) has been utilized to obtain the gridded data from these stations (Pai et al. 2014).

2) DETAILS OF SATELLITE-BASED PRECIPITATION ESTIMATES

The details about the satellite products utilized for the present analysis along with their temporal and spatial resolutions are mentioned in Table 1. These products are as follows.

TABLE 1. Summary of satellite precipitation products.

Station No.	Dataset	Spatial resolution	Temporal resolution	Time period	Data availability	References
1	TMPA 3B42RT V7	0.25° × 0.25°	3 h	Mar 2000 to present	NRT/4-h latency	Huffman et al. (2007, 2010); https://pmm.nasa.gov/data-access/downloads/trmm
2	CMORPH V0.x	0.25° × 0.25°	3 h	Dec 2002 to Oct 2017	1-day latency	Joyce et al. (2004); https://climatedataguide.ucar.edu/climate-data/cmorph-cpc-morphing-technique-high-resolution-precipitation-60s-60n
3	PERSIANN-CDR	0.25° × 0.25°	Daily	Jan 1983 to Sep 2019	4–6-month latency	Ashouri et al. (2015); Hsu et al. (1997); http://chrsdata.eng.uci.edu/
4	IMERG V06B	0.10° × 0.10°	30 min	Jun 2000 to present	NRT (early run)/4-h latency	Huffman et al. (2014); https://pmm.nasa.gov/data-access/downloads/gpm
5	*INSAT-3D* IMR	0.10° × 0.10°	30 min	1 Jun 2014 to present	NRT/6–7-h latency	Kumar and Varma (2017); https://www.mosdac.gov.in/data/metaDataBrowse.do
6	CHIRPS V2.0	0.05° × 0.05°	Daily	1981 to present	NRT/1-day to 3-week latency	Funk et al. (2015); Toté et al. (2015); http://chg.geog.ucsb.edu/data/chirps/
7	PERSIANN-CCS	0.04° × 0.04°	Daily	Jan 2003 to present	NRT/1-h latency	Hsu et al. (1997); http://chrsdata.eng.uci.edu/

(i) TMPA 3B42RT V7

Released in December 2012, TMPA 3B42RT V7 (hereafter, TMPA) is the recent version that has been updated with a new algorithm known to be V7 (Huffman and Bolvin 2014). This dataset provides data at a spatiotemporal resolution of 0.25° × 0.25° and 3-hourly. It is a merged product of multisatellite precipitation available over the globe ranging from 60°S to 60°N in latitude and from 180°W to 180°E in longitude (Huffman et al. 2007, 2010). The TMPA provides two products such as a near-real-time version (TMPA 3B42RT V7) with low latency (4 h) and a post-real-time version with high latency (8 h) known to be TMPA 3B42. TMPA 3B42RT V7 uses passive microwave (MW) and infrared (IR) estimates that are combined by calibrating IR measurements. The 3B42 V7 includes several significant changes over 3B42 V6, including the use of Global Precipitation Climatology Centre (GPCC) analyses and additional satellite data (Huffman and Bolvin 2014). This TMPA version is available from March 2000 to present (near-real-time, hereafter NRT) and is utilized in the present analysis.

(ii) IMERG

IMERG V06B is a day-1 U.S. multisatellite precipitation estimation algorithm for the Global Precipitation Mission (GPM) that is derived from three products: TMPA, CMORPH, and PERSIANN (Huffman et al. 2014). IMERG data are obtainable from an early, a late, and a final run. The early and late run products are available in NRT, with a latency of 4 and 12 h, respectively. The final run product is a post-real-time research product with a latency of about 4 h. In this study, the NRT "early run" product has been considered for the analysis, which is available over the globe ranging from 60°S to 60°N in latitude and from 180°W to 180°E in longitude. This dataset provides data at a high spatiotemporal resolution of 0.1° × 0.1° and half-hourly. IMERG precipitation estimates are computed using passive microwave and infrared satellite sensors. Further, precipitation estimates obtained from passive microwave are rectified using GPM combined instrument product. Finally, monthly rain gauge analyses from the GPCC are used for bias adjustments in the V06B product.

(iii) CMORPH

CMORPH has been developed by Joyce et al. (2004). This algorithm is based on microwave observations, and further, these estimates are interpolated by the motion vectors derived from infrared observations. Using this, precipitation accumulation estimates at different temporal scales (multihours) have been improved compared

to the simple averaging of microwave-based estimates, which incorporate microwave and infrared information. The precipitation estimates are derived from the four types of passive microwave instruments, namely, AMSU-B, AMSR-E (Ferraro et al. 2000), SSM/I (Ferraro 1997), and TMI (Kummerow et al. 2001). CMORPH version 0.x provides the precipitation data at a spatiotemporal resolution of 0.25° × 0.25° and 3-hourly in the range 60°S–60°N in latitude and from 180°W to 180°E in longitude. This is available from December 2002 to October 2017 and has been used for the analysis.

(iv) INSAT-3D

INSAT is a series of multipurpose geostationary satellites developed by the National Oceanic and Atmospheric Administration/Center for Satellite Applications and Research (NOAA/STAR) (Scofield and Kuligowski 2003), launched by the Indian Space Research Organization (ISRO) to achieve the purpose of telecommunications, broadcasting, meteorology, etc. INSAT is the most extensive domestic communication system over the Asia–Pacific region, in which *INSAT-3D* was launched on 26 July 2013 for meteorological applications (Kumar and Varma 2017). There exist numerous established retrievals techniques for *INSAT-3D* derived rain estimation (Barrett and Martin 1981). INSAT Multispectral rainfall (IMR) is the most recent high spatiotemporal rain estimation technique attempted to improve and automat the Interactive Flash Flood Analyzer (IFFA). It gives data in NRT (half-hourly) at a spatial scale of 0.1° × 0.1° (Table 1) in the range 5°–40°N and 60°–100°E. The IMR technique is operationally implemented in *INSAT-3D* for rain estimation.

(v) PERSIANN-CDR

The PERSIANN-CDR has been developed by the Center for Hydrometeorology and Remote Sensing (CHRS) at the University of California, Irvine (UCI) (Ashouri et al. 2015; Hsu et al. 1997). The core of PERSIANN-CDR system estimates rainfall using infrared satellite imagery and ground-surface information using an adaptive artificial neural network (ANN) model. The PERSIANN-CDR has been bias-corrected using the Global Precipitation Climatology Project (GPCP) monthly product version 2.3 (GPCP v2.3) (Sadeghi et al. 2019). It provides daily rainfall estimates at a spatial resolution of 0.25° × 0.25° in the range 60°S–60°N in latitude and 180°W–180°E in longitude from 1983 to 30 September 2019. PERSIANN-CDR is designed to provide a long-term consistent, high spatiotemporal resolution global precipitation dataset, which is aimed at studying the changes in extreme precipitation events due to climate change and natural variability (Mondal et al. 2018).

(vi) CHIRPS

In the present study, the CHIRPS V.2 is utilized. These data have been produced by pentadal rainfall estimates generated from regression models and calibrated using TRMM. Also, stations are blended with the CHIRP data to produce CHIRPS **(**Toté et al. 2015**)**. This product provides data at a spatial resolution of 0.05° × 0.05° with a latency from 1 day to 3 weeks that are available over the globe in the range 50°S–50°N, 180°E–180°W and are available from 1981 to NRT at pentadal (5-day total rainfall), decadal (10-day total rainfall), and monthly temporal resolution (Funk et al. 2015).

(vii) PERSIANN-CCS

PERSIANN-CCS is developed by the Center for CHRS at the University of California, Irvine (UCI) (Hsu et al. 1997). It provides NRT data at a high spatial resolution of 0.04° × 0.04° and daily scale with a latency of 1 h, in the range of 60°S–60°N, 180°E–180°W. Satellite precipitation product PERSIANN-CCS system facilitates the categorization of cloud-patch features based on the areal extent, cloud height, and variability of texture evaluated from satellite imagery. PERSIANN-CCS uses a cloud segmentation algorithm with a variable threshold that identifies and separates patches of clouds. The patches are then classified based on different properties, texture, and dynamic evolution (Hong et al. 2004). These classifications assign rainfall values to pixels based on the relationship between rain rate and brightness temperature (Hong et al. 2004).

The IMD rainfall and satellite estimates have different scales in both temporal and spatial domains. Indian standard time (IST) is 5 h and 30 min ahead of Coordinated Universal Time (UTC).

Rainfall observations in India are monitored every 3-hourly from 0300 UTC of the previous day to 0300 UTC of the present day. Whereas, satellite estimates are obtained from 0000 UTC. For a fair comparison between satellite estimates with observations, satellite data (available at an hourly scale) are considered from the same time as observations (i.e., from 0300 UTC). However, as some of the satellites provide data at a daily level, it is not possible to make UTC adjustment for them. Therefore, these satellite estimates are rescaled to the hourly scale. A simple procedure is followed for the same. Let R_{i-1} and R_i be the amount of rainfall on $(i-1)$th and ith day, respectively. For this purpose, it is assumed that R follows a uniform distribution, that is, $R \sim U(0, 24)$, the probability density of R is given as

$$f(r) = \left\{ \begin{array}{l|l} \dfrac{1}{24-0} & 0 \le r \le 24 \\ 0 & \text{otherwise} \end{array} \right\}. \quad (1)$$

Further, UTC adjustment is made in the following way:

$$6\left(\frac{3r_{i-1}}{24}\right) + 2\left(\frac{3r_i}{24}\right) = \frac{3r_{i-1} + r_i}{4}. \quad (2)$$

According to the day definition of rain gauge data, there are six and two data points at a 3-h scale of the previous day and present day, respectively. Therefore, the first $6(3r_{i-1}/24)$ indicates a cumulative sum of six data points at a 3-h scale of the previous day and accordingly, the second term indicates. Finally, the term $(3r_{i-1} + r_i)/4$ shows that satellite estimates can be comparable with gauge-based observations on a particular day.

In this method, it is assumed that rainfall is distributed uniformly over each time (hour). It may induce some biases in the representation of actual rainfall, that is, time scale experiencing extreme rainfall may be treated as normal. This limitation can be resolved in the following way: Satellite estimates at daily scale are partitioned into eight data points at a 3-h scale. On a particular day (ith), the amount of rainfall is estimated by considering six data points at a 3-h scale of the $(i - 1)$ th day and two data points of ith day. The information lost (amount of rainfall) during the ith day is added to $(i + 1)$th day. That is the amount of rain recorded for 18 h is cumulated into the next day. The use of IPOD (refer to section 2) resolves this problem as it keeps 12–24 h as a buffer in both directions. So, the rainfall extremes can be captured by the use of IPOD, and no biases will be induced.

Finally, both the datasets are compared at a common temporal scale, that is, daily for an event analysis.

Also, for comparative analysis, the satellites datasets are rescaled using bilinear interpolation method on the same spatial resolution 0.25° × 0.25° as of IMD gridded data. However, two finescale resolution satellite products, namely, CHIRPS (0.05° × 0.05°), and PERSIANN-CCS (0.04° × 0.04°) are evaluated against gauge station data as IMD gridded data of resolution 0.25° × 0.25° will be too coarse to compare with finescale estimates.

The details about the satellite products, along with their temporal and spatial resolutions, are mentioned in Table 1.

c. Details of events

The focus of the present study is an assessment of 18 cloudburst events that were reported in media during 2014–16 over NWH (Dimri et al. 2017). For the facilitation of uniformity between observed and satellite data, the period of the present analysis is taken from 2014 to 2016. Societal impact, loss of lives, and destruction reported was the primary prerequisite required for choosing these cloudburst events (Table 2). The spatial locations of these events are shown in Fig. 1 over the NWH region along with 77 functional stations of IMD.

1) CALCULATION OF THE RAINFALL THRESHOLDS

The percentile threshold is calculated thus:

1) The 95th, 98th, and 99.99th percentile value (prc) of the daily rainfall is calculated for three different states HP, U.K., and J&K, that is, we calculated $\text{prc}^j_{i,k}$, where $i = \{1, 2, 3\} = \{\text{J\&K, HP, U.K., and NWH}\}$, respectively, $j = \{95, 98, 99.99\}$ percentiles, and $k = 1, 2, \ldots, n$ (total number of grids of the corresponding region).
2) The prc is obtained over time 1998–2016.
3) $\text{thr}_i = \sum_{k=1}^{n} \text{prc}^j_{i,k}/n$, $i = \{1, 2, 3\}$; $j = \{95, 98, 99.99\}$.

The rainfall thresholds associated with the percentiles 95th, 98th, and 99.99th are calculated as 13.95, 25.8, and 137.71 mm day^{-1}, respectively, for the whole of NWH and also separately for each region (Table 3). The calculated thresholds at different percentiles suggest that there is a significant variation in the rainfall amount within the NWH region. It may be due to the strength and monsoonal path of action. As the monsoon strength decreases from south to north along the mountain barrier and east to west along a monsoonal way (Basistha et al. 2008), U.K. experiences high percentile values followed by HP and J&K as seen in Table 3.

2) STATISTICAL MEASURES

The statistical measures employed in the present work for comparative analysis are listed in the appendix.

3) IMPROVED POD: A NEW METRIC

In this work, it has been discerned that observed gridded and satellite-based estimates lag by certain time units. The method of probability of detection (POD) finds the probability of occurrence of an event above a threshold by satellite estimates w.r.t. reference data. It assumes that an event is detected by the reference and satellite estimates at the same time point. However, it may happen that satellite estimates would detect an event after a particular time step. This is quite possible as every satellite estimate has some latency time. Therefore, the present work incorporates this time gap using a new metric defined as improved POD.

The improved POD (IPOD) is defined as

TABLE 2. Location of the reported events.

Station No.	Date	Location (lat/lon)	Altitude (m)	Damage (loss of lives, property)	Reference (newspaper/author)
1	7–9 Aug 2015	Dharampur, HP (31.899°N, 77.019°E)	1482	5 humans	*India Today*, *Daily Bhaskar*, 8 Aug 2015
2	25 Jul 2015	Banjar, Kullu, HP (31.63°N, 77.34°E)	1356	Not reported (NR)	*The Times of India*, 25 Jul 2015
3	8 Aug 2015	Dharampur, Mandi, HP (31.7°N, 76.7°E)	1189		
4	1–7 Sep 2014	Srinagar, J&K (34.084°N, 74.797°E)	1585	215 humans	*Down To Earth*, 18 Oct 2014
5	23 Jul 2015	Mendhar, Poonch, J&K (33.60°N, 74.14°E)	1580	19 structures, 5 houses, 11 mud houses	*Rising Kashmir*, 29 Jul 2015
6	16 Jul 2015	Sonamarg, J&K (34.40°N, 74.71°E)	2800	4 humans	*Indian Express*, 17 Jul 2015
7	12 Jul 2015	Pahalgam, J&K (34.01°N, 75.31°E)	2740	2 humans	*PTI*, 13 Jul 2015
8	17 Jul 2015	Ganderbal, J&K (34.21°N, 74.77°E)	1619	3 humans	*Daily Excelsior*, 17 Jul 2015
9	24 Jul 2015	Baltal, J&K (34.6°N, 74.7°E)	2743	Not reported (NR)	*PTI*, 24 Jul 2015
10	28 Jul 2015	Choskore village, J&K (34.19°N, 76.35°E)	4361	20 houses	*Kashmir Life*, *Greater Kashmir*, 29 Jul 2015
11	28 Jul 2015	Wakha village, J&K (34.16°N, 77.6°E)	3710	20 houses	*Kashmir Life*, *Greater Kashmir*, 29 Jul 2015
12	22–28 Jul 9 Aug 2015	Baima, J&K (34.15°N, 77.57°E)	3898	Office-cum-residence of Water and Power Consultancy Services (WAPCOS) damage	*Kashmir Life*, 10 Aug 2015
13	4 Aug 2015	Uppar Ganglass, Saboo, J&K (34.31°N, 77.53°E)	4149	NR	National Institute of Hydrology (NIH)
14	3 Jun–2 Jul 2016	Pithoragarh, U.K. (30.081°N, 80.365°E)	1514	30 humans	*New 18th*, 2 Jul 2016
15	20 Aug 2016	Marchula, Pauri, U.K. (29.606°N,79.092°E)	1814	7 humans	*The Indian Express*, 21 Aug 2016
16	28 May 2016	Kemra, U.K. (30.57°N, 78.68°E)	2212	120 houses, 100 animals	*Millennium Post*, 29 May 2016
17	28 May 2016	Siliara, U.K. (30.46°N, 78.62°E)	2175	120 houses, 100 animals	*Millennium Post*, 29 May 2016
18	14–15 Aug 2014	Purala, Pauri, U.K. (30.147°N, 78.775°E)	1524	16 humans	*The Indian Express*, 16 Aug 2016

TABLE 3. Rainfall amount associated with 95th, 98th, and 99.99th percentiles for NWH, U.K., HP, and J&K.

Region	95th	98th	99.99th
NWH	13.95	25.8	137.71
U.K.	20.8	36.3	162.85
HP	16.88	29.28	142.2
J&K	11.85	22.42	130.61

$$\text{IPOD} = \frac{A}{(A + C)}, \tag{3}$$

where A and C are redefined as

$$A = I[(\text{imd}_i \geq \text{thr}) \,\&\, (\text{sat}_j \geq \text{thr})], \quad i = t, \quad j \in (t-1, t+1), \tag{4}$$

and

$$C = I[(\text{imd}_i \geq \text{thr}) \,\&\, (\text{sat}_i < \text{thr})]. \tag{5}$$

Parameter I is the indicator function for the success of a hit, defined as $I_A(x) = 1$, if, $x \in A$ and 0, if $x \notin A$.

Similarly, for the false alarm, it is defined as

$$I_C(x) = 1, \quad \text{if} \quad x \in C, \quad \text{and} \quad 0, \quad \text{if} \quad x \notin C. \tag{6}$$

Here, the interval of the localized time domain is taken as $(t - 1, t + 1)$. The value 1 represents a one-unit time forward shift, while -1 is for one-unit time backward shift from a particular time t. The one-unit shift refers to one day in both forward and backward direction over the time axis as the study considered daily data for the evaluation and comparison analysis. It implies that at a certain time t, three consecutive data points, that is, the rainfall intensity of satellites, at $t - 1$, t, and $t + 1$ are compared with the observed rainfall intensity at t.

3. Results and discussion

In this work, IMD gridded data are assessed for 18 cloudburst events taken from media and literature. At the same time, the performance analysis of satellite estimates is done on the locations wherein IMD gridded has performed successfully.

a. Evaluation of IMD gridded data

The IMD gridded data at daily scale are evaluated based on two parameters such as accumulated and maximum rainfall amount obtained at the location of 18 events. The accumulated rainfall is the sum of the amount during an event period considering the effect of adjacent grids to incorporate the cumulative impact of rain in nearby locations (Bharti and Singh 2015). Thus, accumulated rainfall shows the spatial distribution and reveals the location of the cloudburst events. In contrast, maximum rainfall refers to the highest amount obtained during an event period and displayed in the bar plot.

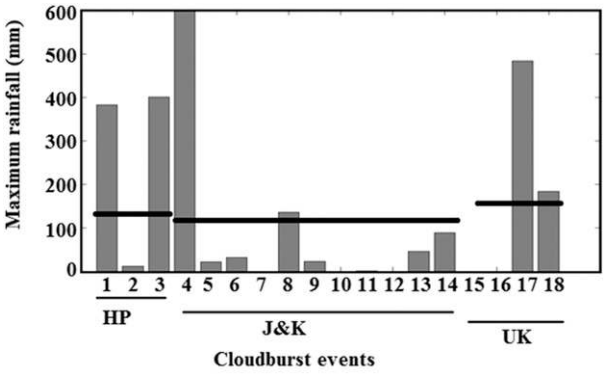

FIG. 2. Maximum rainfall during an event period obtained from IMD gridded data against a regional threshold. The thick horizontal line shows the 99.99th percentile threshold value of the corresponding region. The numbers on the x axis correspond to the cloudburst events mentioned in Table 2.

1) MAXIMUM RAINFALL OBTAINED BY IMD DATA

The exact amount of rainfall from ground stations is not available for the 18 events as few occurred at ungauged locations. We assume that these were the cloudbursts based on the destruction caused as reported in the media. Therefore, we aim to evaluate the merits of IMD gridded data using the regional threshold obtained at the 99.99th percentile from 19 years of data (Table 3). The maximum rainfall is the highest amount captured at a grid location, which has been estimated by gridded data during the temporal period of each event. Figure 2 represents the maximum rainfall of 18 events against the regional threshold. If this threshold is crossed at an event location, the event is assumed to be captured by the IMD. Our results reveal that IMD data could capture the rainfall amount for six events at Solan, Srinagar, Pithoragarh, Mandi, Pahalgam, and Purala. That is, IMD gridded data can capture 33% of the events, which may vary based on the sample size. The maximum rainfall obtained from IMD gridded data at these six event locations is shown in Table 4.

2) SPATIAL DISTRIBUTION OF IMD GRIDDED DATA

The accumulated rainfall is calculated for the 18 cloudburst events, and it is demonstrated that IMD can pinpoint the location of six events, as shown in Fig. 3. It is estimated that the event at Srinagar received the

TABLE 4. Maximum rainfall that occurred during the cloudburst events. Rainfall amount that has crossed the 99.99th percentile is marked in bold.

Station No.	Location	IMD	TMPA	CMORPH	PERSIANN-CDR	IMERG	*INSAT-3D*	CHIRPS	PERSIANN-CCS
1	Solan	**382.7**	**152.85**	1.09	90.38	1.85	0	**214.37**	**264.91**
2	Mandi	**400.8**	**139.03**	0.015	50.41	0.1	0	70.90	97.32
3	Srinagar	**598.8**	**400.28**	66.03	**266.38**	40.31	38.04	**406.45**	68.14
4	Pahalgam	**135.9**	23.94	1.50	1.91	1.44	0	0	9.21
5	Pithoragarh	**484.1**	**292.65**	15.82	111.57	105.87	13.85	**510.45**	**134.83**
6	Purala	**184.5**	**120.38**	0.31	107.27	0	0	**258.60**	**263.33**

highest accumulated rainfall of ~598.6 mm, Mandi (~400.8 mm), Solan (~382.7 mm), Pahalgam (~135.9 mm), Pithoragarh (~484.1 mm), and lowest in Purala (~184 mm). It is noticed that there are a few IMD stations within the range of event location at Srinagar, but the rainfall amount above a regional threshold is captured by the gridded data. On the contrary, there are large numbers of rain gauge stations available around the Banjar; however, this event location is not captured by the gridded data. The possible reasons could be the location of the rain gauge station or low maintenance of the station. It may be noted that there are only a few instances at which nearby stations around Srinagar missed to report the rainfall amount during the event period, as shown in Table 5. On the other hand, it is found that during an event period at Banjar (Table 6), most of the stations have provided missing values during extreme rainfall events. Similar observations are also seen in other events at which IMD gridded data fails to capture the events. Therefore, more than establishing a dense network, IMD is required to take proper attention toward the quality of station data and also for technical maintenance over remote hilly terrain. Further, we evaluate satellites at these six locations for the entire time where IMD has performed well.

b. Performance analysis of satellite products

The performance of satellite estimates is assessed through maximum precipitation, the spatial distribution of accumulated precipitation, and contingency information such as POD, VHI, and FAR.

1) MAXIMUM PRECIPITATION OBTAINED BY SATELLITE ESTIMATES

The maximum precipitation captured by satellites during the 18 events is estimated, and the values at six locations where IMD has performed well are shown in Table 4. It shows that the precipitation retrieved from the

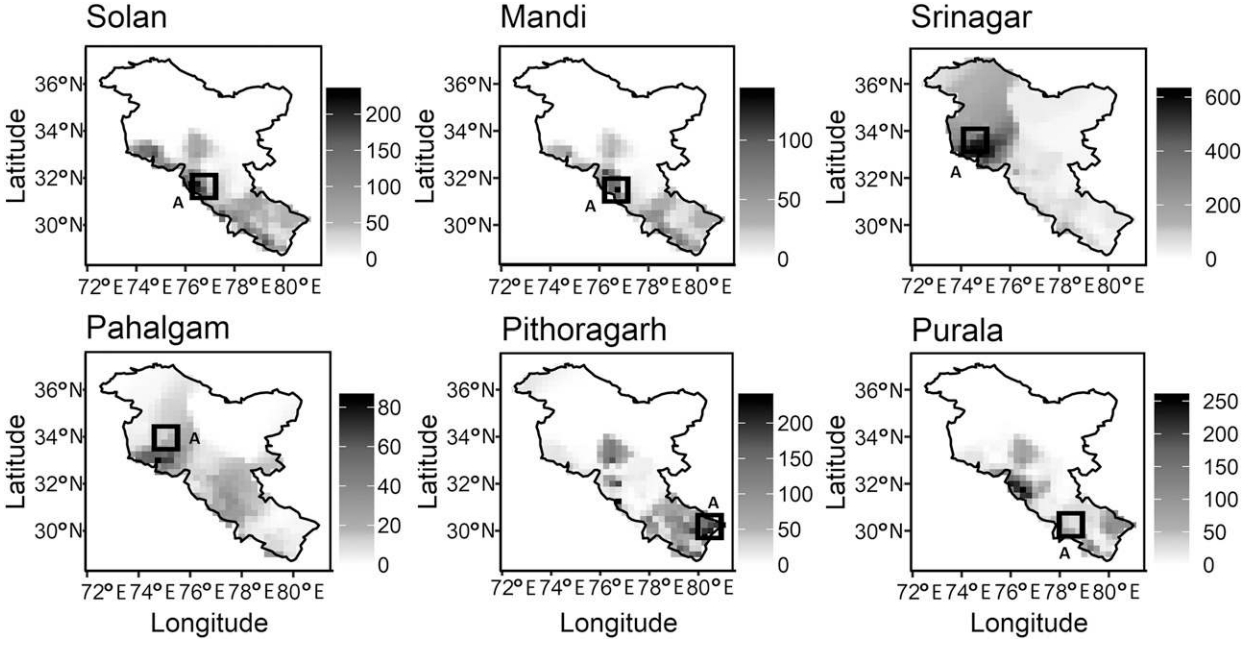

FIG. 3. Spatial location of six cloudburst events as detected by IMD data. Here, the bar represents the accumulated rainfall (mm).

TABLE 5. Data from rain gauge stations around Srinagar, J&K (34.084°N, 74.797°E), during the cloudburst event.

Station	Distance (km)	1 Sep 2014	2 Sep 2014	3 Sep 2014	4 Sep 2014	5 Sep 2014	6 Sep 2014	7 Sep 2014
Anantnag	51.4	10.6	6.4	58.4	180	—	—	—
Pahalgam	53.6	33.4	3.2	40.2	58.6	—	—	—
Gulmarg	39.8	0	0.6	34	106.6	128	98.2	—
Qazi	57.8	8.2	7.3	80.4	156.7	156.7	206	—
Kupwara	59.4	2.3	1.8	2.8	45.6	68.2	15.4	—
Banihal	68.8	0.4	15.6	93.7	106.8	188.8	86.1	53.8
Srinagar	32.8	13.6	0.4	20	51.8	0	—	—

satellites such as *INSAT-3D*, CMORPH, and IMERG underestimated the maximum rainfall that occurred during the events. In turn, these three satellites are unable to detect any of the cloudburst events. Overall, TMPA detected five cloudburst events at Solan, Mandi, Srinagar, Pithoragarh, and Purala, whereas CHIRPS detected four cloudburst events at Solan, Srinagar, Purala, and Pithoragarh. Therefore, it is concluded that TMPA and CHIRPS capture 27.7% and 22.2% of the total events. Similarly, PERSIANN-CCS could capture three events, that is, Solan, Pithoragarh, and Purala with a success rate of 16.67%, while PERSIANN-CDR has 16.67% success rate to capture such events (Srinagar, Pithoragarh, and Purala).

2) SPATIAL DISTRIBUTION OF SATELLITE ESTIMATES

The relative bias (RB) index between satellite estimates and IMD is calculated using Eq. (A1). In Fig. 4a, it is shown that the TMPA and PERSIANN-CDR could locate the event at Srinagar, although they overestimated the amount of IMD rainfall by 37.2% and 26.7%, respectively. The *INSAT-3D* and IMERG have highest RB (−91%) followed by the CMORPH (−62.2%). Figure 4b shows that TMPA captured the location of the event at Mandi with RB (8.8%) followed by PERSIANN-CDR (−60%), whereas other satellites underestimated with RB approximately −90.9%. Further, Fig. 4c reveals that satellites captured the event at Pithoragarh with RB index as TMPA (−36.0%), CMORPH (−93.4%), PERSIANN-CDR (−67.9%), IMERG (−52.8%), and *INSAT-3D* (−96.2%). It is found that all the satellites underestimated the event at Pithoragarh. However, TMPA has relatively less RB value as compared with other satellites. Similarly, TMPA and PERSIANN-CDR overestimated the accumulated rainfall at Purala with RB value 27.8% and 55.9%, respectively, as shown in Fig. 4d. Similarly, other satellite estimates like IMERG, *INSAT-3D*, and CMORPH produce significantly high RB (−100%) at Purala (Fig. 4d) events. It is concluded that based on the index of RB, the performance of TMPA in detecting the accumulated rainfall during the event period is better in comparison with others followed by PERSIANN-CDR.

3) CONTINGENCY STATISTICS

The performance of satellites to detect a given rainfall amount is achieved by evaluating the contingency information in terms of different statistics. In the present study, the contingency information of satellites is calculated at six cloudburst locations over the entire time domain (2014–16). The statistics of contingency information such as POD, volumetric hit index (VHI), and false alarm ratio (FAR) are calculated using Eqs. (A2) and (A3) over the cloudburst locations and shown in Figs. 5–7, respectively. POD shows the probability of

TABLE 6. Data from rain gauge stations around Banjar, HP (31.63°N, 77.34°E), during the cloudburst event.

Station	Distance (km)	25 Jul 2015
Bilaspur	66.2	—
Ghumarwin	66.5	—
Hamirpur	81.3	0
Sujanpur	86.3	0
Palampur	95.2	0
Nichar	62.5	—
Sangla	94.6	—
Banjar	6.7	0
Bhuntar	26.9	0.2
Kullu	39.4	—
Manali	65.5	0
Keylong	99.9	0
Janjehli	17.7	5
Jhungi	35.6	—
Jogindernagar	65.3	16.5
Karsog	28.6	0
Mandi	38.8	6.9
Sundernagar	47.1	0.8
Pachhad	93.0	—
Rajgarh	91.1	0
Arki	61.8	0
Dharampur	80.1	2
Kandaghat	70.8	0
Kasauli	84.1	13
Nalagarh	85.6	—
Solan	76.5	0

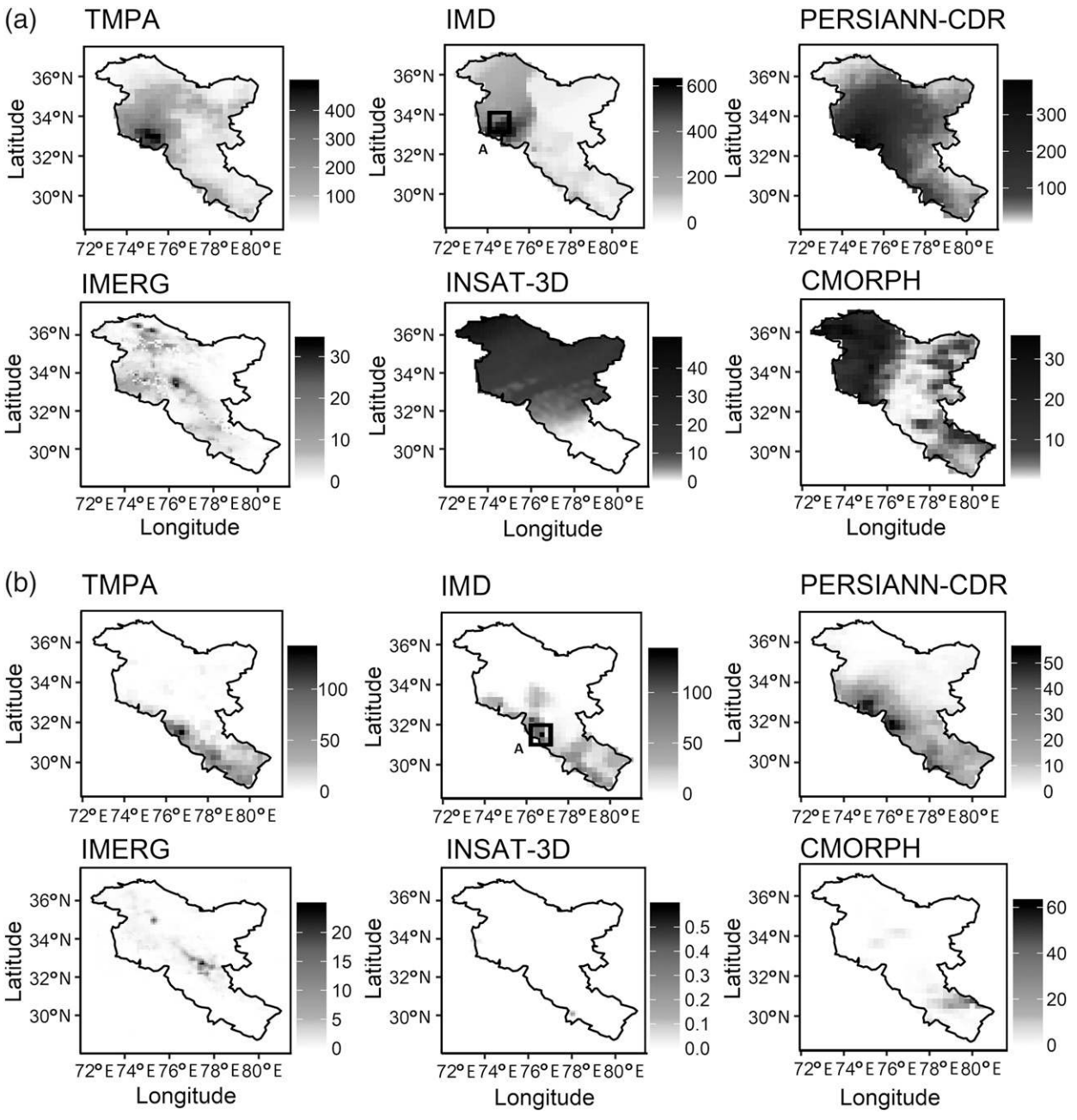

FIG. 4. Spatial location of cloudburst event at (a) Srinagar as detected by satellite data. The bar represents the accumulated rainfall (mm). (b) As in (a), but for Mandi. (c) As in (a), but for Pithoragarh. (d) As in (a), but for Purala.

success to detect rainfall events at various percentiles. In contrast, VHI explores the ability of satellite estimates to capture the fraction of rainfall occurring over an event location. Further, FAR gives the information of false detection about the satellites. The POD is calculated over 95th to 99.99th percentiles at six cloudburst locations for five satellites where IMD gridded data was able to detect the event. The results are shown in Fig. 5 and it reveals that the probability of satellites to detect an event decreases as the amount of rainfall from 95th to 99.99th percentile increases. It is seen that all satellites can detect 99.99th percentile rainfall; however, these probabilities vary over the events. For example, at Solan, it is seen that POD of PERSIANN-CDR is 78.7% at the 95th percentile, and it decreases to 72.0% at the 99.99th percentile. Also, POD of PERSIANN-CDR is 81.0% at the 95th percentile at Mandi, and it decreases to 76.0% at the 99.99th percentile. It is observed that

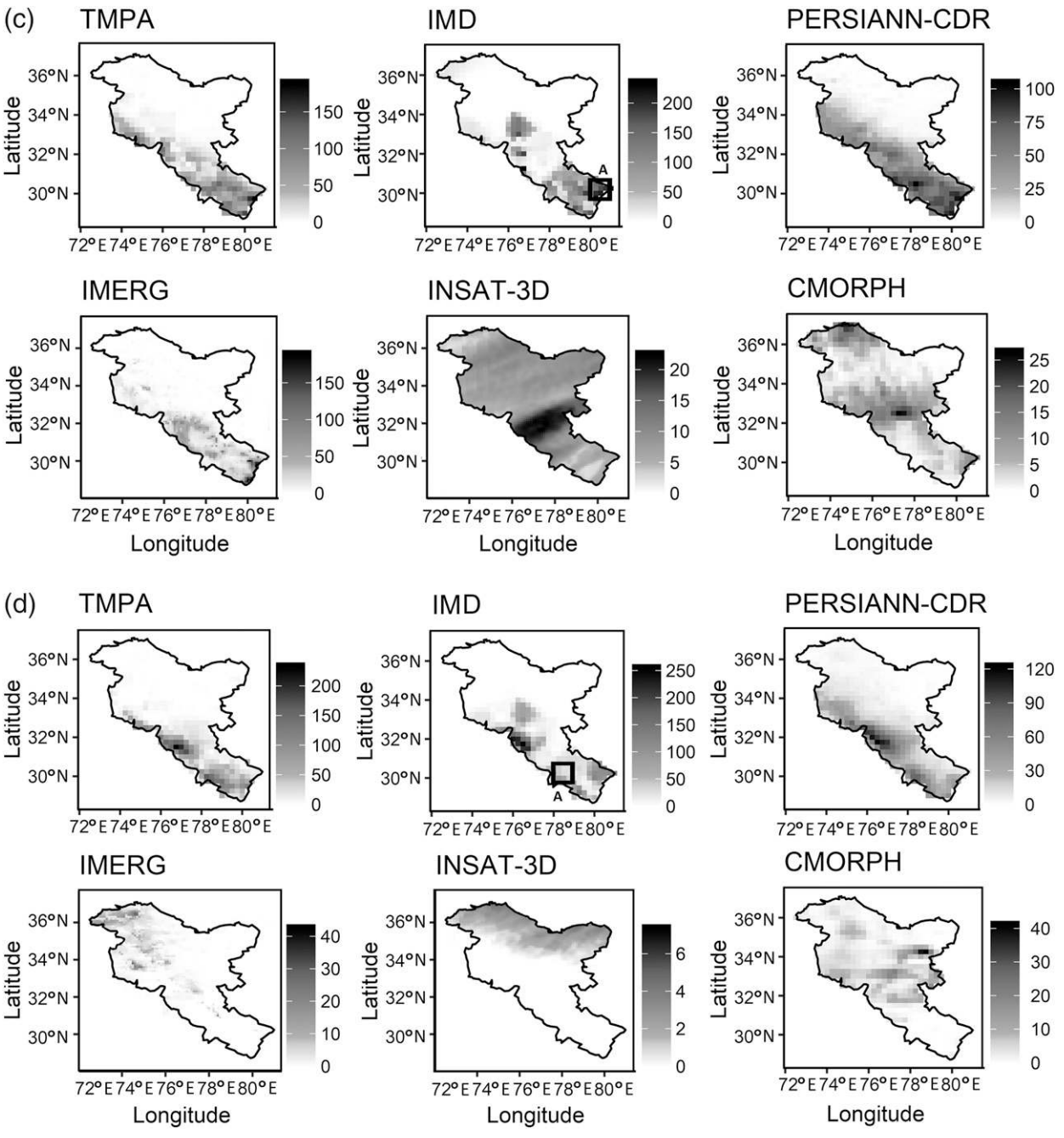

FIG. 4. (*Continued*)

this satellite performed uniformly in the detection of rainfall extremes overall events followed by TMPA and IMERG. Also, it is noticed that the *INSAT-3D* performed very poorly in the detection of rainfall extremes followed by CMORPH.

The extended version of contingency information such as VHI is calculated over time (2014–16) and is shown in Fig. 6. The results reveal that the PERSIANN-CDR captures the highest fraction of the volume of rainfall in comparison with other satellites at 99.99th percentile overall events except at Purala. The range of VHI for PERSIANN-CDR at the 95th percentile is observed to be between 56.0% and 86.5%, and it decreases to 46.3%–82.1% at the 99.99th percentile. However, the performance of PERSIANN-CDR in capturing rainfall fraction over the percentiles is consistent except at Purala. Similarly, the range of VHI for TMPA at the 95th percentile is observed to be between 35.8%

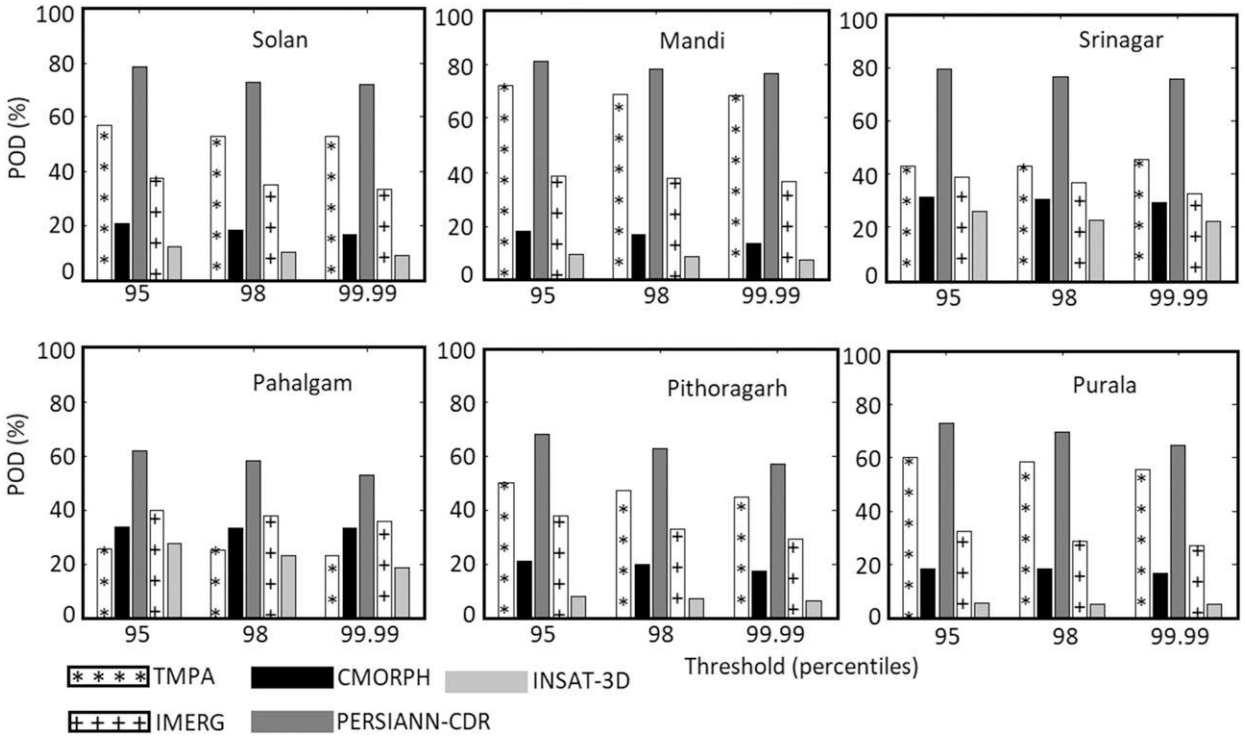

FIG. 5. The POD of satellites at six cloudburst locations calculated over entire time period 2014–16. The *x* axis represents the rainfall threshold calculated at 95th–99.99th percentiles.

and 84.7%, while the range is decreased to 33.4%–81.5% at the 99.99th percentile. Further, TMPA receives the highest rainfall fraction at Mandi (81.5%) followed by 64.4% and 64.2%, at Purala and Solan events, respectively. Also, it is observed that IMERG captures a significant amount of fraction (36.9%) of rainfall occurring at the Mandi event.

Further, the FAR of the satellites is calculated, and the corresponding results are shown in Fig. 7. It reveals that at the 99.99th percentile level, the range of FAR of TMPA is 43.4%–82.0% over the cloudburst events, in which the lowest (43.4%) and highest FAR (82.0%) values are noticed at Pahalgam and Mandi, respectively. Similarly, the range of FAR of PERSIANN-CDR is about 43.6%–68.2% over the cloudburst events, in which the lowest is at Pahalgam and highest at Mandi. CMORPH has the highest (41.6%) FAR value at the event Pithoragarh and the lowest value at Purala (20.3%).

The distribution of POD over the geographical stretch of NWH is presented in the box-and-whisker plot, as shown in Fig. 8a, and the median of the distribution is shown in Fig. 8b. It reveals that the range of POD distribution decreases, that is, the median of distribution decreases with increasing rainfall threshold from 95th to 99.99th percentiles. The satellite *INSAT-3D* performs very poorly in detecting the rainfall extremes followed by CMORPH. In contrast, TMPA has the highest (34.11%) median value of POD distribution at 99.99th percentile level, followed by PERSIANN-CDR (33.4%) and IMERG (11.3%).

Similarly, VHI is calculated, and the results are shown in the box-and-whisker plot presented in Fig. 9. It is observed that the rainfall amount captured by satellites reduces as the percentile level increases from 95th to 99.99th. For example, the median of VHI distribution for TMPA reduces from 48.4% to 44.7% as rainfall threshold increases from the 95th to 99.99th percentile. The median value of VHI distribution suggests that PERSIANN-CDR captures the highest rainfall amount (32.2%) at the 99.99th percentile, followed by IMERG (13.7%). It is found that *INSAT-3D* performs very poorly followed by CMORPH. These poor values of metrics may be due to the high variability of precipitation in space and time, and it shows that satellite data are in agreement with observations only up to a certain time lag. Taking this temporal variation into account, it is assumed that the satellite products might be following the observed phenomenon in a different localized time. So, a new metric, defined as IPOD is calculated to see the improvement in the detection of extreme events.

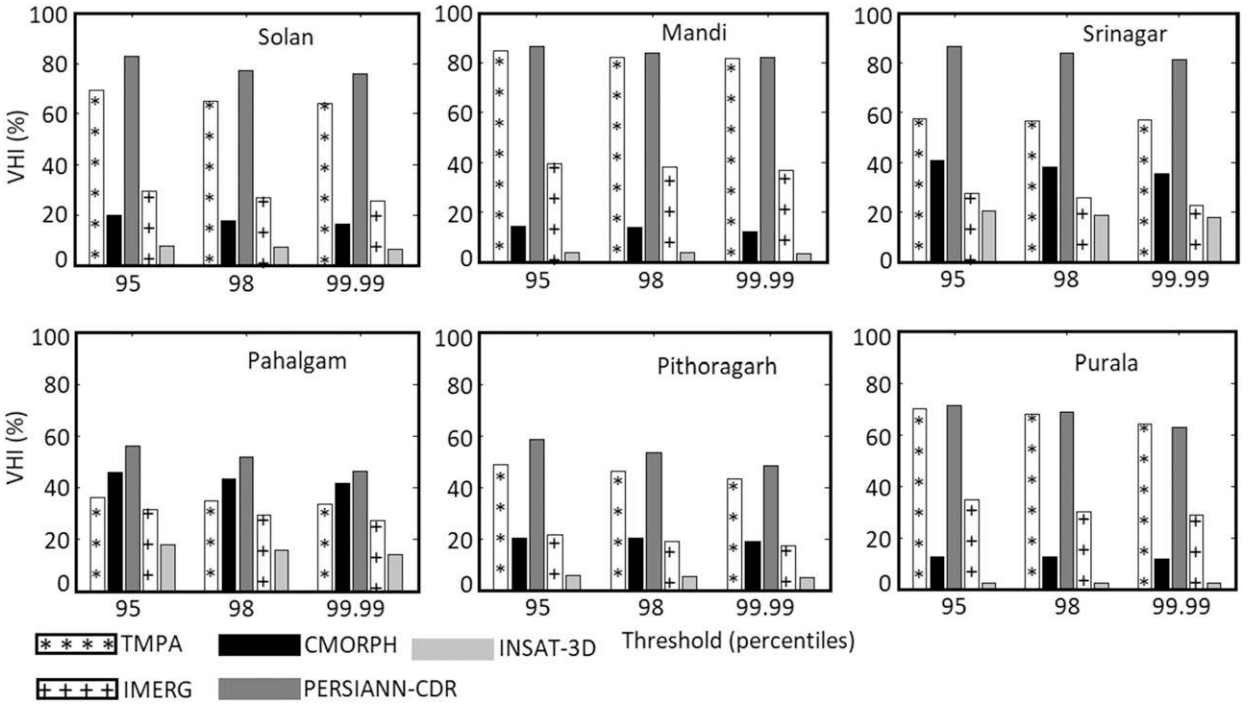

FIG. 6. The VHI of satellites at six cloudburst locations. The *x* axis represents the rainfall threshold calculated at 95th–99.99th percentiles.

The IPOD of satellites over six selected cloudburst events are calculated using Eqs. (3)–(6) and the corresponding results are shown in Fig. 10. The result reveals that an improvement in POD is seen for TMPA, IMERG, and PERSIANN-CDR at all percentile levels. For example, the range of IPOD of TMPA at the 95th percentile is obtained to be 41.8%–81.9%, while it was 25.43%–71.9% in the standard POD case. In case of the 99.99th percentile, the range of IPOD is estimated to be 39.6%–78.9%, whereas it was 23.13%–68.16% in standard POD. Similarly, a transition is seen in POD to IPOD in PERSIANN-CDR with range variation from 52.976.4% to 70.0%–86.0% at the 99.99th percentile. Also, IMERG experiences such changes from POD to IPOD with a range from 26.9%–36.5% to 40.9–57.9% at the 99.99th percentile. Likewise, CMORPH and *INSAT-3D* experience change, as depicted in Fig. 10.

The results of IPOD over the geographical stretch of NWH are shown in Fig. 11a, whereas the median of the distribution is depicted in Fig. 11b. It reveals that there is an improvement in the detection of rainfall extremes from 95th to 99.99th by all satellites. The range of IPOD of TMPA at 95th percentile is obtained to be 38.6%–75.8%, while it is 22.4%–58.5% in the standard POD case. In the case of the 99.99th percentile, the range of IPOD is estimated to be 32.7%–74.4%, whereas it is 19.4%–53.9% in standard POD. Similarly, a transition is seen in standard POD to IPOD in PERSIANN-CDR with range variation from 31.6%–57.14% to 51.9%–76.6%. Also, IMERG experiences such changes from standard POD to IPOD with a range from 4.9%–17.8% to 15.2%–39.0% at the 99.99th percentile.

c. *Performance analysis of finescale resolution satellites*

We have performed our analysis of previous sections on the fine resolution data available from CHIRPS and PERSIANN-CCS at 0.05° × 0.05°and 0.04° × 0.04° resolution, respectively. The results obtained at six locations against IMD nearby station data are shown in Fig. 12. It is seen that the performance of CHIRPS in the detection of rainfall extremes is consistent overall percentiles. Further, the results obtained from IPOD reveals that the performance in the detection of rainfall extremes at the 99.99th percentile of CHIRPS is highest (78.6%) at Srinagar, whereas it shows lowest IPOD of 60.5% at Pithoragarh. Similarly, PERSIANN-CCS detects the cloudburst event with the highest IPOD of 77.17% at Srinagar and the lowest 56.9% at Pithoragarh. Comparing these results with satellite estimates of coarser resolutions, it is concluded that the finescale satellite estimates perform quite well in the detection of rainfall extremes. Our results are summarized in Fig. 13.

4. Discussion and conclusions

Evaluation of high-resolution data for monitoring the events such as cloudbursts since they facilitate mayhem

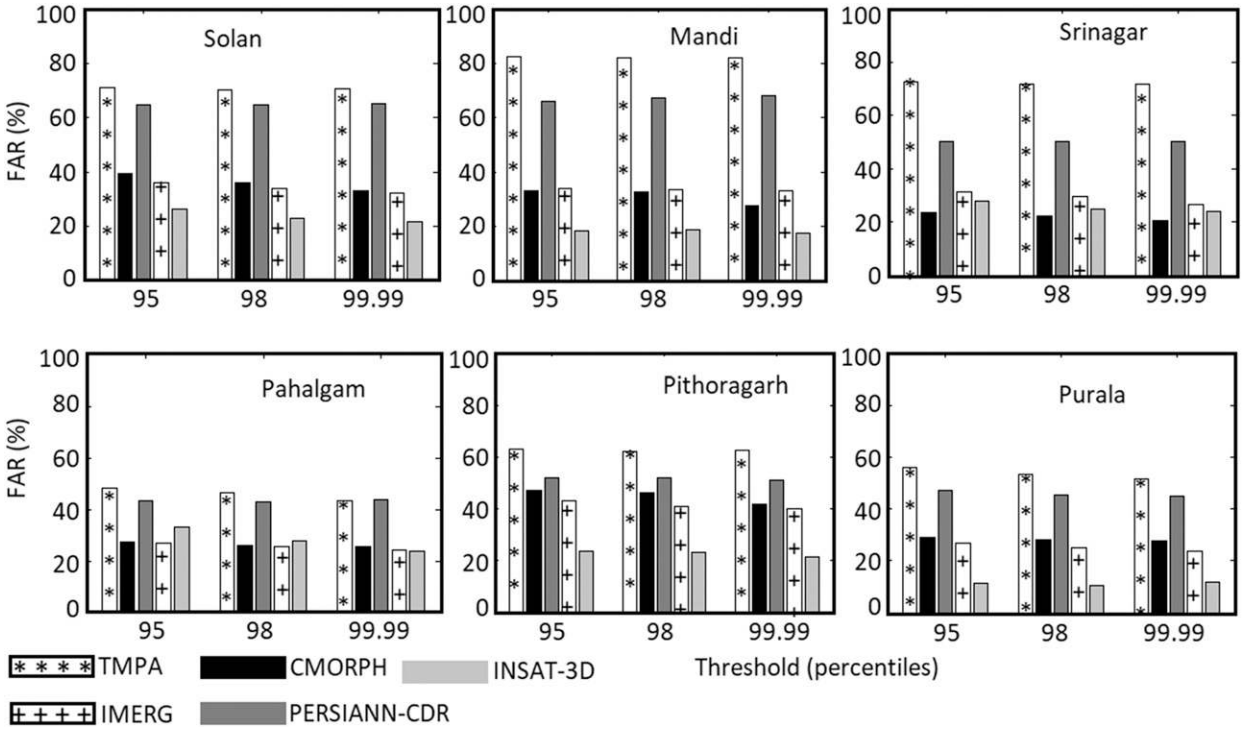

FIG. 7. The FAR index of all satellites at cloudburst locations. The *x* axis represents the rainfall threshold calculated at 95th–99.99th percentiles.

in the region is of utmost necessity. The critical concern in the assessment of IMD gridded data is the only observed source beneficial in the detection and prediction of these events at ungauged locations. As a result, the present paper emphasizes the importance of evaluating IMD high-resolution gridded observed data as well as satellites like CHIRPS and PERSIANN-CCS, which have not been evaluated over NWH region, particularly for cloudburst events.

Critical rainfall thresholds are generally used for the identification of extreme events that correspond to a level above which the event may take place. The cloudburst events presented in this work are taken from the media assuming they have crossed a 99.99th percentile

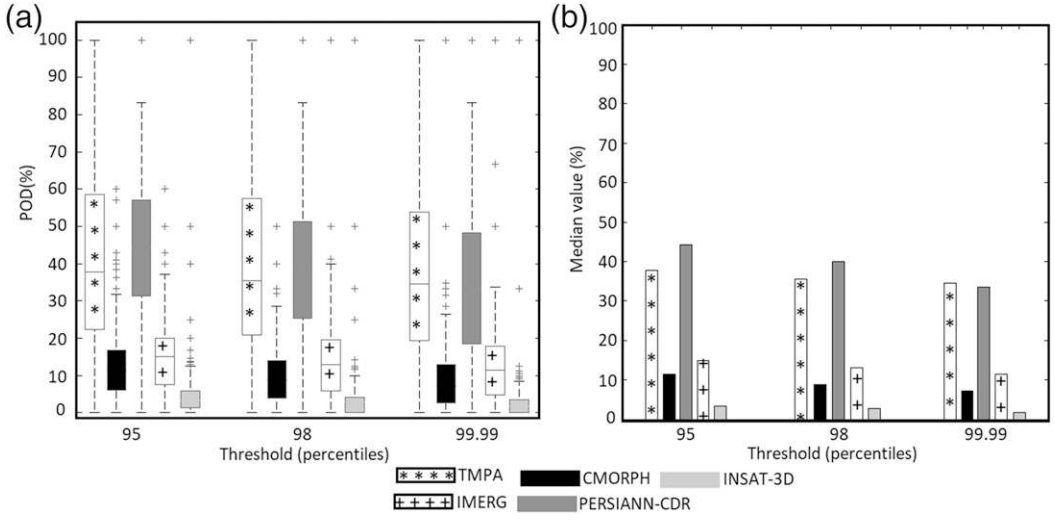

FIG. 8. (a) The distribution of POD at the geographical stretch of NWH; (b) median value of the POD. The *x* axis represents the rainfall threshold calculated at 95th–99.99th percentiles.

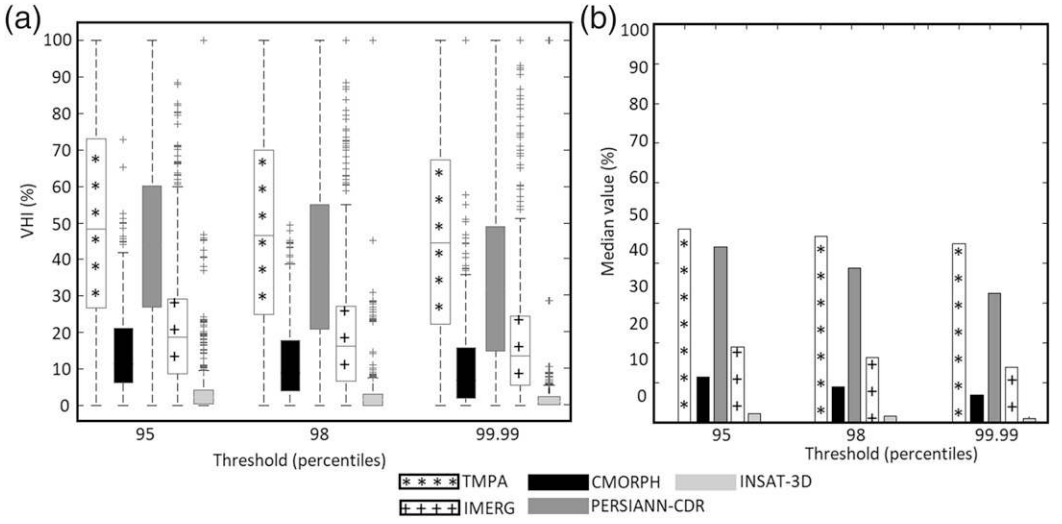

FIG. 9. (a) The distribution of VHI at geographical stretch of NWH; (b) median value of the VHI. The *x* axis represents the rainfall threshold calculated at 95th–99.99th percentiles.

value that statistically defines a cloudburst event. These thresholds are calculated as 130.61 mm for J&K, 142.2 mm for HP, and 162.8 mm for the U.K. from 19 years IMD data. Through such regional thresholds, a conclusion is drawn stating that out of 18 reported cloudburst events, IMD gridded data can detect six events. The main reason behind the poor performance of the gridded set could be the low density of rain gauge stations, or nonclimatic influences in remote areas like maintenance, quality control, drift correction, station replacement, etc. To obtain more reliable climate data in such locations, besides the possibility of establishing dense stations, an improvement in interpolation techniques and station maintenance should be addressed for increasing the quality of the data.

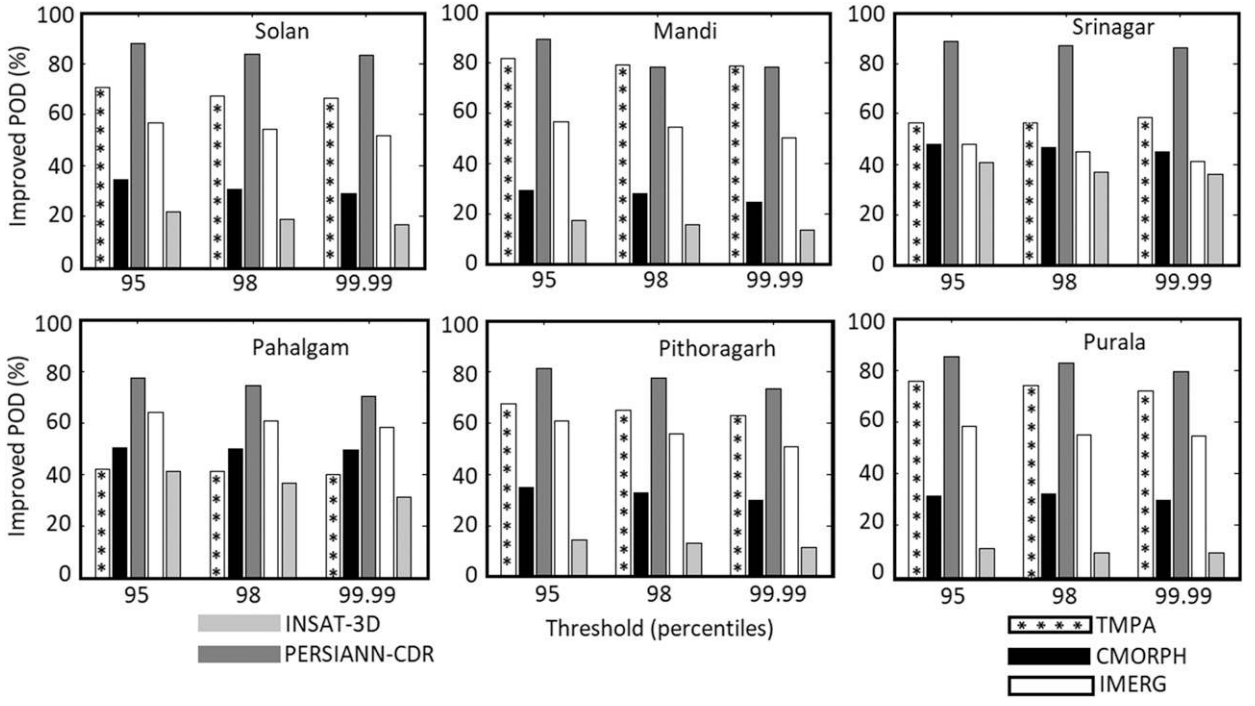

FIG. 10. IPOD at each of the cloudburst event. The *x* axis represents the rainfall threshold calculated at 95th–99.99th percentiles.

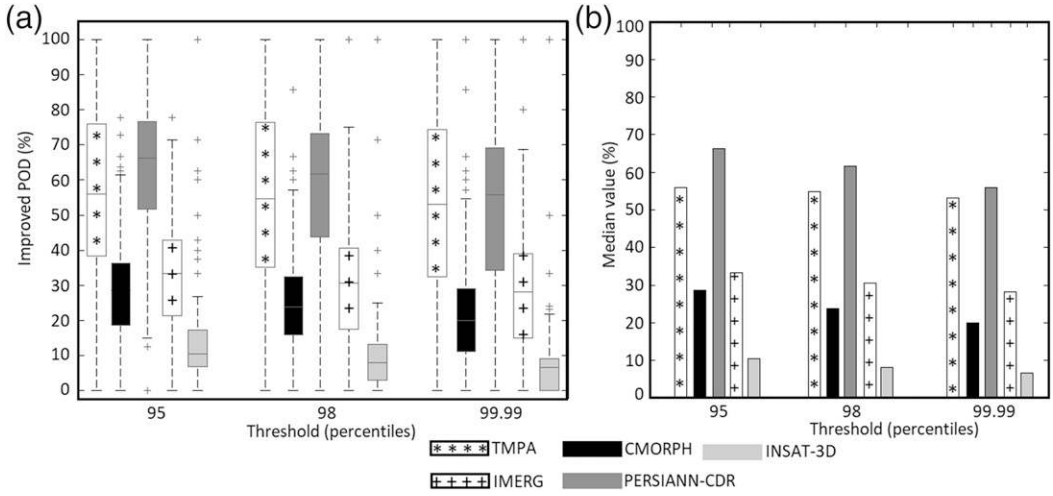

FIG. 11. (a) The distribution of IPOD at geographical stretch of NWH; (b) median value. The *x* axis represents the rainfall threshold calculated at 95th–99.99th percentiles.

Further, we have evaluated the performance of seven satellites on the locations where IMD data has performed well. Therein it is assumed that IMD gridded data has captured all the rainfall events associated with the 99.99th percentile at these locations for the period 2014–16. Thereby contingency information like POD, VHI, FAR values is calculated at six locations for the entire period. The influence of time lag in the satellite data is adjusted through a new metric defined as IPOD. In the standard POD, the method does not consider the temporal lag between the two datasets. But it may happen that a satellite would detect an event after a particular time step. Therefore, the present work incorporates this time gap using IPOD.

The following conclusions are drawn at the 99.99th percentile:

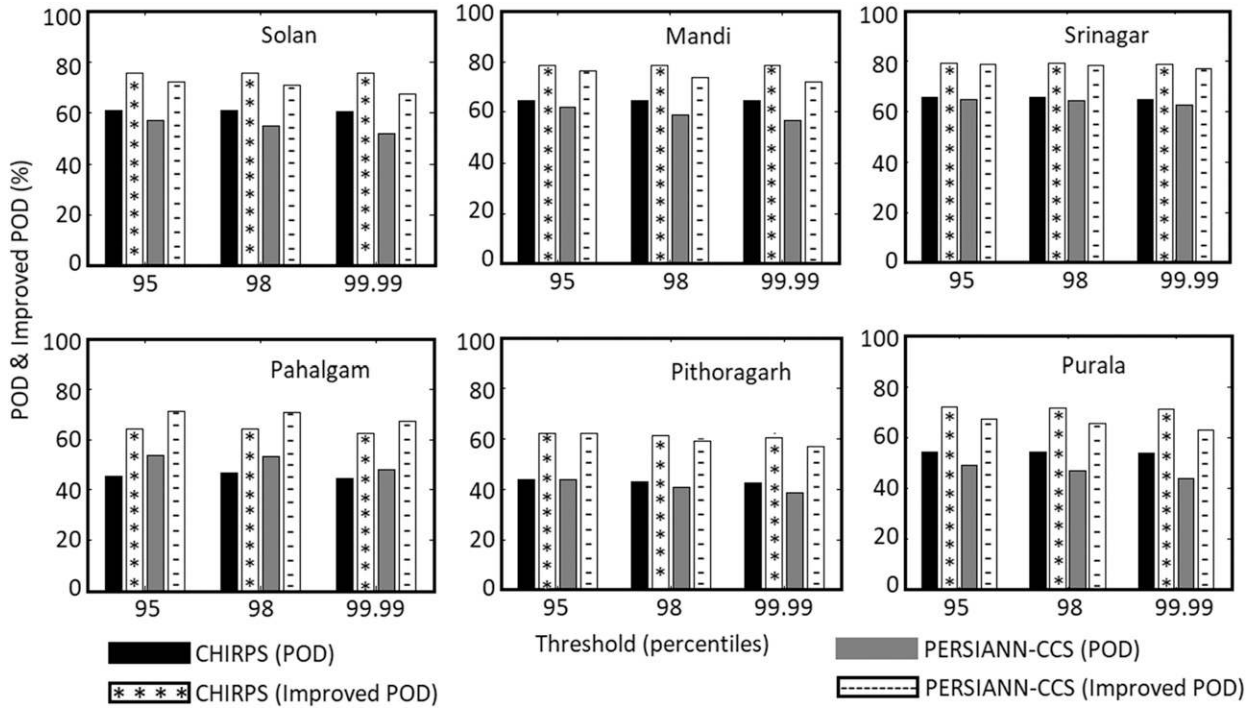

FIG. 12. POD and IPOD obtained from fine-resolution satellites.

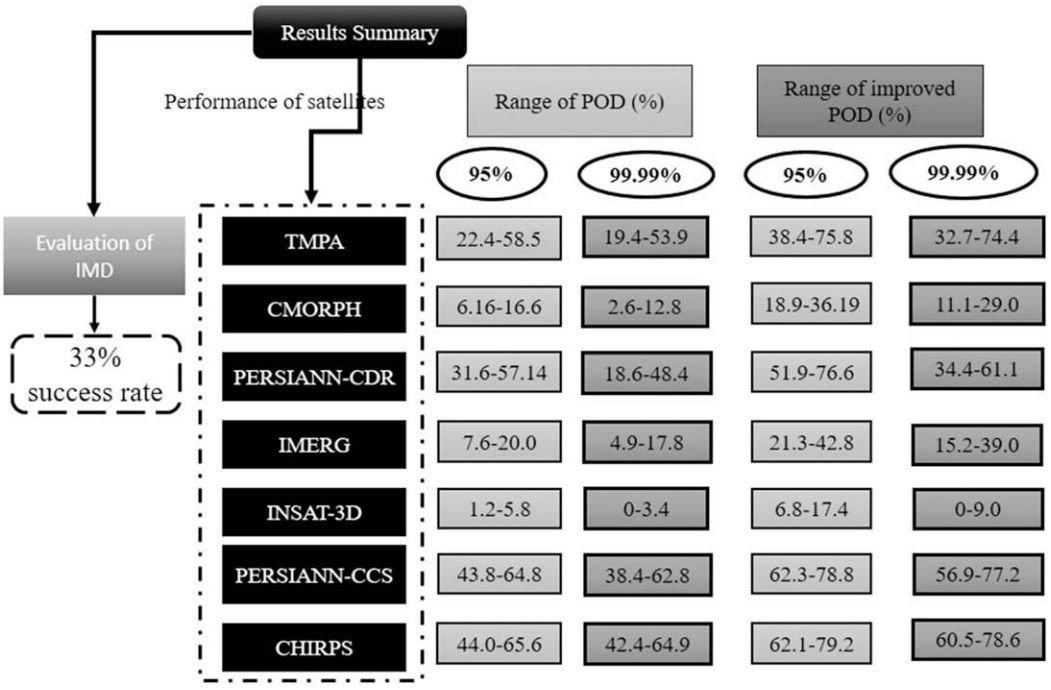

FIG. 13. Summary of the performance of satellite estimates.

- The range of POD of TMPA is 19.4%–53.9%, followed by PERSIANN-CDR (18.6%–48.4%) and IMERG (4.9%–17.8%) over the NWH.
- Using IPOD metric, the performance of the satellite in detecting the cloudburst event is enhanced. The range of IPOD of TMPA is 32.8%–74.4%, followed by PERSIANN-CDR (34.4%–69.11%) and IMERG (15.3%–39.0%).
- The median value of standard POD distribution in TMPA is 37.8%, whereas it is 55.9% in IPOD.
- Finescale satellite product CHIRPS can detect a cloudburst event with a probability of 60.5%–78.6% using IPOD metric.

Acknowledgments. The authors wish to thank IITM and IMD, Pune, India for sharing the rain gauge and gridded data for the analysis. Authors' contributions: P.J. developed the methodology, generated all the results, wrote the initial draft, and did analysis and necessary correction. S.G. did data collection and the preprocessing part. S.A. conceived the idea and did correction and final analysis of the manuscript.

APPENDIX

Statistical Measures

The statistic metrics used in the present analysis are relative bias (RB) and the probability of detection (POD). RB is defined as follows:

$$\mathrm{RB} = \frac{(\text{satellite} - \text{IMD})}{\text{IMD}} \times 100. \tag{A1}$$

The measure RB is a dimensionless quantity used to quantify the overestimation and underestimation after multiplying by 100. Similarly, the other measures are defined as (Dinku et al. 2010; Wilks 2006)

$$\mathrm{POD} = \frac{A}{A + C} \tag{A2}$$

and

$$\mathrm{FAR} = \frac{B}{A + C}. \tag{A3}$$

Equation (A2) gives the fraction of observations detected correctly by the satellites. The range of POD and FAR lies in between 0 and 1; the value of 0 gives that the satellite has no skill to detect rainfall events whereas 1 indicates a high score of the satellite.

In Eqs. (A2) and (A3), A, B, and C represent number of hits, false alarms, and miss rate, respectively.

TABLE A1. Contingency information of the satellites (obs = observed and sat = satellite).

	Obs ≥ threshold	Obs < threshold
Sat ≥ threshold	A	B
Sat < threshold	C	D

Hit means both the observation and the satellite detect the cloudburst events, whereas false alarm means the observation missed but the satellite detects and miss rate *C* refers to events detected by observation but missed by the satellites. The contingency information of the satellites is mentioned in the Table A1.

The statistics calculated from the Eq. (A2) provides the performance of the satellites based on the categorical measures. For example, a POD of 0.9 indicates that the satellites detect 90% of events. However, it fails to provide information about the fraction of the volume of precipitation detected by the satellites. For this reason, one may need to improve the statistical score obtained by the original contingency table metrics and estimate the fraction of the total volume of the climate variables of interest detected correctly. Therefore, the extended version of the Eq. (A2) is proposed by (AghaKouchak and Mehran 2013). The volumetric hit index (VHI), which is the extended version of the POD, can be defined as follows:

$$\mathrm{VHI} = \frac{\sum_{i=1}^{n} (\mathrm{sat}_i | \mathrm{obs}_i > \mathrm{thr} \,\&\, \mathrm{sat}_i > \mathrm{thr})}{\sum_{i=1}^{n} (\mathrm{sat}_i | \mathrm{obs}_i > \mathrm{thr} \,\&\, \mathrm{sat}_i > \mathrm{thr}) + \sum_{i=1}^{n} (\mathrm{obs}_i | \mathrm{obs}_i > \mathrm{thr} \,\&\, \mathrm{sat}_i \le \mathrm{thr})}, \tag{A4}$$

where sat refers to satellite observations being evaluated, whereas obs represents observations. In Eq. (A4), *n* is the sample size, which is the total number of events, considered in this study, and thr is the threshold value. The value of VHI lies between 0 and 1 in which 1 is the perfect score.

REFERENCES

Aadhar, S., and V. Mishra, 2017: High-resolution near real-time drought monitoring in South Asia. *Sci. Data*, **4**, 170145, https://doi.org/10.1038/sdata.2017.145.

AghaKouchak, A., and A. Mehran, 2013: Extended contingency table: Performance metrics for satellite observations and climate model simulations. *Water Resour. Res.*, **49**, 7144–7149, https://doi.org/10.1002/wrcr.20498.

Ashouri, H., K. L. Hsu, S. Sorooshian, D. K. Braithwaite, K. R. Knapp, L. D. Cecil, B. R. Nelson, and O. P. Prat, 2015: PERSIANN-CDR: Daily precipitation climate data record from multisatellite observations for hydrological and climate studies. *Bull. Amer. Meteor. Soc.*, **96**, 69–83, https://doi.org/10.1175/BAMS-D-13-00068.1.

Barrett, E. C., and D. W. Martin, 1981: *Use of Satellite Data in Rainfall Monitoring*. Academic Press, 34 pp.

Basistha, A., D. S. Arya, and N. K. Goel, 2008: Spatial distribution of rainfall in Indian Himalayas–A case study of Uttarakhand region. *Water Resour. Manage.*, **22**, 1325–1346, https://doi.org/10.1007/s11269-007-9228-2.

Beck, H. E., T. R. McVicar, A. I. van Dijk, J. Schellekens, R. A. de Jeu, and L. A. Bruijnzeel, 2011: Global evaluation of four AVHRR–NDVI data sets: Intercomparison and assessment against Landsat imagery. *Remote Sens. Environ.*, **115**, 2547–2563, https://doi.org/10.1016/j.rse.2011.05.012.

Beria, H., T. Nanda, D. S. Bisht, and C. Chatterjee, 2017: Does the GPM mission improve the systematic error component in satellite rainfall estimates over TRMM? An evaluation at a pan-India scale. *Hydrol. Earth Syst. Sci.*, **21**, 6117–6134, https://doi.org/10.5194/hess-21-6117-2017.

Bharti, V., and C. Singh, 2015: Evaluation of error in TRMM 3B42V7 precipitation estimates over the Himalayan region. *J. Geophys. Res. Atmos.*, **120**, 12 458–12 473, https://doi.org/10.1002/2015JD023779.

——, ——, J. Ettema, and T. A. R. Turkington, 2016: Spatiotemporal characteristics of extreme rainfall events over the Northwest Himalaya using satellite data. *Int. J. Climatol.*, **36**, 3949–3962, https://doi.org/10.1002/joc.4605.

Chen, C., Q. Chen, Z. Duan, J. Zhang, K. Mo, Z. Li, and G. Tang, 2018: Multiscale comparative evaluation of the GPM IMERG v5 and TRMM 3B42 v7 precipitation products from 2015 to 2017 over a climate transition area of China. *Remote Sens.*, **10**, 944, https://doi.org/10.3390/rs10060944.

Chevuturi, A., A. P. Dimri, S. Das, A. Kumar, and D. Niyogi, 2015: Numerical simulation of an intense precipitation event over Rudraprayag in the central Himalayas during 13–14 September 2012. *J. Earth Syst. Sci.*, **124**, 1545–1561, https://doi.org/10.1007/s12040-015-0622-5.

Dahiya, G., P. Jena, S. Garg, and S. Azad, 2020: Inter-comparison of high-resolution satellite estimates for cloudburst events in the Northwest Himalaya. *Himalayan Weather and Climate and Their Impact on the Environment*, A. P. Dimri et al., Eds., Springer, 3–17.

Das, S., R. Ashrit, and M. W. Moncrieff, 2006: Simulation of a Himalayan cloudburst event. *J. Earth Syst. Sci.*, **115**, 299–313, https://doi.org/10.1007/BF02702044.

Derin, Y., and K. K. Yilmaz, 2014: Evaluation of multiple satellite-based precipitation products over complex topography. *J. Hydrometeor.*, **15**, 1498–1516, https://doi.org/10.1175/JHM-D-13-0191.1.

Dimri, A. P., and S. K. Dash, 2012: Wintertime climatic trends in the western Himalayas. *Climatic Change*, **111**, 775–800, https://doi.org/10.1007/s10584-011-0201-y.

——, A. Chevuturi, D. Niyogi, R. J. Thayyen, K. Ray, S. N. Tripathi, A. K. Pandey, and U. C. Mohanty, 2017: Cloudbursts in Indian Himalayas: A review. *Earth-Sci. Rev.*, **168**, 1–23, https://doi.org/10.1016/j.earscirev.2017.03.006.

Dinku, T., P. Ceccato, E. Grover-Kopec, M. Lemma, S. J. Connor, and C. F. Ropelewski, 2007: Validation of satellite rainfall products over East Africa's complex topography. *Int. J. Remote Sens.*, **28**, 1503–1526, https://doi.org/10.1080/01431160600954688.

——, F. Ruiz, S. J. Connor, and P. Ceccato, 2010: Validation and intercomparison of satellite rainfall estimates over Colombia. *J. Appl. Meteor. Climatol.*, **49**, 1004–1014, https://doi.org/10.1175/2009JAMC2260.1.

——, K. Hailemariam, R. Maidment, E. Tarnavsky, and S. Connor, 2014: Combined use of satellite estimates and rain gauge

observations to generate high-quality historical rainfall time series over Ethiopia. *Int. J. Climatol.*, **34**, 2489–2504, https://doi.org/10.1002/joc.3855.

Feidas, H., 2010: Validation of satellite rainfall products over Greece. *Theor. Appl. Climatol.*, **99**, 193–216, https://doi.org/10.1007/s00704-009-0135-8.

Ferraro, R. R., 1997: Special sensor microwave imager derived global rainfall estimates for climatological applications. *J. Geophys. Res.*, **102**, 16 715–16 735, https://doi.org/10.1029/97JD01210.

——, F. Weng, N. C. Grody, and L. Zhao, 2000: Precipitation characteristics over land from the NOAA-15 AMSU sensor. *Geophys. Res. Lett.*, **27**, 2669–2672, https://doi.org/10.1029/2000GL011665.

Funk, C., and Coauthors, 2015: The climate hazards infrared precipitation with stations - a new environmental record for monitoring extremes. *Sci. Data*, **2**, 150066, https://doi.org/10.1038/sdata.2015.66.

Goswami, B. N., V. Venugopal, D. Sengupta, M. S. Madhusoodanan, and P. K. Xavier, 2006: Increasing trend of extreme rain events over India in a warming environment. *Science*, **314**, 1442–1445, https://doi.org/10.1126/science.1132027.

Goswami, P., and K. V. Ramesh, 2008: Extreme rainfall events: Vulnerability analysis for disaster management and observation system design. *Curr. Sci.*, **98**, 1037–1044.

Guhathakurta, P., O. P. Sreejith, and P. A. Menon, 2011: Impact of climate change on extreme rainfall events and flood risk in India. *J. Earth Syst. Sci.*, **120**, 359–373, https://doi.org/10.1007/s12040-011-0082-5.

Herrera, S., J. M. Gutiérrez, R. Ancell, M. R. Pons, M. D. Frías, and J. Fernández, 2012: Development and analysis of a 50-year high-resolution daily gridded precipitation dataset over Spain (Spain02). *Int. J. Climatol.*, **32**, 74–85, https://doi.org/10.1002/joc.2256.

Hessels, T. M., 2015: Comparison and validation of several open access remotely sensed rainfall products for the Nile Basin. M.S. thesis, Dept. of Water Management, Delft University of Technology, 233 pp., http://resolver.tudelft.nl/uuid:3566f883-16fd-4465-be43-6b2037baa6ff.

Hofstra, N., M. New, and C. McSweeney, 2010: The influence of interpolation and station network density on the distributions and trends of climate variables in gridded daily data. *Climate Dyn.*, **35**, 841–858, https://doi.org/10.1007/s00382-009-0698-1.

Hong, Y., K. Hsu, S. Sorooshian, and X. Gao, 2004: Precipitation estimation from remotely sensed imagery using an artificial neural network cloud classification system. *J. Appl. Meteor.*, **43**, 1834–1853, https://doi.org/10.1175/JAM2173.1.

——, D. Gochis, J. T. Cheng, K. L. Hsu, and S. Sorooshian, 2007: Evaluation of PERSIANN-CCS rainfall measurement using the NAME event rain gauge network. *J. Hydrometeor.*, **8**, 469–482, https://doi.org/10.1175/JHM574.1.

Houze, R. A., Jr., 2012: Orographic effects on precipitating clouds. *Rev. Geophys.*, **50**, RG1001, https://doi.org/10.1029/2011RG000365.

Hsu, K., X. Gao, S. Sorooshian, and H. V. Gupta, 1997: Precipitation estimation from remotely sensed information using artificial neural networks. *J. Appl. Meteor.*, **36**, 1176–1190, https://doi.org/10.1175/1520-0450(1997)036<1176:PEFRSI>2.0.CO;2.

Huffman, G. J., and D. T. Bolvin, 2014: TRMM and other data precipitation data set documentation. NASA TRMM Doc., 42 pp., http://precip.gsfc.nasa.gov/pub/trmmdocs/3B42_3B43_doc.pdf.

——, and Coauthors, 2007: The TRMM Multisatellite Precipitation Analysis (TMPA): Quasi-global, multiyear, combined-sensor precipitation estimates at fine scales. *J. Hydrometeor.*, **8**, 38–55, https://doi.org/10.1175/JHM560.1.

——, R. F. Adler, D. T. Bolvin, and E. J. Nelkin, 2010: The TRMM multi-satellite precipitation analysis (TMPA). *Satellite Rainfall Applications for Surface Hydrology*, Springer, 3–22.

——, D. T. Bolvin, D. Braithwaite, K. Hsu, R. Joyce, and P. Xie, 2014: NASA Global Precipitation Measurement Integrated Multi-satellitE Retrievals for GPM (IMERG). Algorithm Theoretical Basis Doc., version 4.4, 26 pp., https://pps.gsfc.nasa.gov/Documents/IMERG_ATBD_V4.pdf.

Joyce, R. J., J. E. Janowiak, P. A. Arkin, and P. Xie, 2004: CMORPH: A method that produces global precipitation estimates from passive microwave and infrared data at high spatial and temporal resolution. *J. Hydrometeor.*, **5**, 487–503, https://doi.org/10.1175/1525-7541(2004)005<0487:CAMTPG>2.0.CO;2.

Katsanos, D., A. Retalis, and S. Michaelides, 2016: Validation of a high-resolution precipitation database (CHIRPS) over Cyprus for a 30-year period. *Atmos. Res.*, **169**, 459–464, https://doi.org/10.1016/j.atmosres.2015.05.015.

Kumar, B., K. C. Patra, and V. Lakshmi, 2016: Daily rainfall statistics of TRMM and CMORPH: A case for trans-boundary Gandak River basin. *J. Earth Syst. Sci.*, **125**, 919–934, https://doi.org/10.1007/s12040-016-0710-1.

Kumar, P., and A. K. Varma, 2017: Assimilation of INSAT-3D hydro-estimator method retrieved rainfall for short-range weather prediction. *Quart. J. Roy. Meteor. Soc.*, **143**, 384–394, https://doi.org/10.1002/qj.2929.

Kummerow, C., and Coauthors, 2001: The evolution of the Goddard Profiling Algorithm (GPROF) for rainfall estimation from passive microwave sensors. *J. Appl. Meteor.*, **40**, 1801–1820, https://doi.org/10.1175/1520-0450(2001)040<1801:TEOTGP>2.0.CO;2.

Mei, Y., E. N. Anagnostou, E. I. Nikolopoulos, and M. Borga, 2014: Error analysis of satellite precipitation products in mountainous basins. *J. Hydrometeor.*, **15**, 1778–1793, https://doi.org/10.1175/JHM-D-13-0194.1.

Mishra, A. K., 2013: Effect of rain gauge density over the accuracy of rainfall: A case study over Bangalore, India. *SpringerPlus*, **2**, 311, https://doi.org/10.1186/2193-1801-2-311.

Mitra, A. K., I. M. Momin, E. N. Rajagopal, S. Basu, M. N. Rajeevan, and T. N. Krishnamurti, 2013: Gridded daily Indian monsoon rainfall for 14 seasons: Merged TRMM and IMD gauge analyzed values. *J. Earth Syst. Sci.*, **122**, 1173–1182, https://doi.org/10.1007/s12040-013-0338-3.

——, N. Kaushik, A. K. Singh, S. Parihar, and S. C. Bhan, 2018: Evaluation of INSAT-3D satellite derived precipitation estimates for heavy rainfall events and its validation with gridded GPM (IMERG) rainfall dataset over the Indian region. *Remote Sens. Appl. Soc. Environ.*, **9**, 91–99, https://doi.org/10.1016/j.rsase.2017.12.006.

Mondal, A., V. Lakshmi, and H. Hashemi, 2018: Intercomparison of trend analysis of multisatellite monthly precipitation products and gauge measurements for river basins of India. *J. Hydrol.*, **565**, 779–790, https://doi.org/10.1016/j.jhydrol.2018.08.083.

Nair, S., G. Srinivasan, and R. Nemani, 2009: Evaluation of multisatellite TRMM derived rainfall estimates over a western state of India. *J. Meteor. Soc. Japan*, **87**, 927–939, https://doi.org/10.2151/jmsj.87.927.

Nandargi, S., and O. N. Dhar, 2012: Extreme rainstorm events over the northwest Himalayas during 1875–2010. *J. Hydrometeor.*, **13**, 1383–1388, https://doi.org/10.1175/JHM-D-12-08.1.

Orlanski, I., 1975: A rational subdivision of scales for atmospheric processes. *Bull. Amer. Meteor. Soc.*, **56**, 527–530, https://doi.org/10.1175/1520-0477-56.5.527.

Pai, D. S., L. Sridhar, M. Rajeevan, O. P. Sreejith, N. S. Satbhai, and B. Mukhopadhyay, 2014: Development of a new high spatial resolution (0.25° × 0.25°) long period (1901–2010) daily gridded rainfall data set over India and its comparison with existing data sets over the region. *Mausam*, **65**, 1–18.

Parida, B. R., S. N. Behera, O. Bakimchandra, A. C. Pandey, and N. Singh, 2017: Evaluation of satellite-derived rainfall estimates for an extreme rainfall event over Uttarakhand, Western Himalayas. *Hydrology*, **4**, 22, https://doi.org/10.3390/hydrology4020022.

Prakash, S., V. Sathiyamoorthy, C. Mahesh, and R. M. Gairola, 2014: An evaluation of high-resolution multisatellite rainfall products over the Indian monsoon region. *Int. J. Remote Sens.*, **35**, 3018–3035, https://doi.org/10.1080/01431161.2014.894661.

——, A. K. Mitra, I. M. Momin, D. S. Pai, E. N. Rajagopal, and S. Basu, 2015: Comparison of TMPA-3B42 versions 6 and 7 precipitation products with gauge-based data over India for the southwest monsoon period. *J. Hydrometeor.*, **16**, 346–362, https://doi.org/10.1175/JHM-D-14-0024.1.

——, ——, A. AghaKouchak, Z. Liu, H. Norouzi, and D. S. Pai, 2018: A preliminary assessment of GPM-based multi-satellite precipitation estimates over a monsoon dominated region. *J. Hydrol.*, **556**, 865–876, https://doi.org/10.1016/j.jhydrol.2016.01.029.

Qin, Y., Z. Chen, Y. Shen, S. Zhang, and R. Shi, 2014: Evaluation of satellite rainfall estimates over the Chinese Mainland. *Remote Sens.*, **6**, 11 649–11 672, https://doi.org/10.3390/rs61111649.

Rahman, S. H., D. Sengupta, and M. Ravichandran, 2009: Variability of Indian summer monsoon rainfall in daily data from gauge and satellite. *J. Geophys. Res.*, **114**, D17113, https://doi.org/10.1029/2008JD011694.

Rajeevan, M., J. Bhate, and A. K. Jaswal, 2008: Analysis of variability and trends of extreme rainfall events over India using 104 years of gridded daily rainfall data. *Geophys. Res. Lett.*, **35**, L18707, https://doi.org/10.1029/2008GL035143.

Rao, V. K., A. K. Mitra, K. K. Singh, G. Bharathi, R. R. Kumar, K. Ray, and S. Ramakrishna, 2020: Evaluation of INSAT-3D derived TPW with AIRS retrievals and GNSS observations over the Indian region. *Int. J. Remote Sens.*, **41**, 1139–1169, https://doi.org/10.1080/01431161.2019.1657604.

Roy Bhowmik, S. K., and A. K. Das, 2007: Rainfall analysis for Indian monsoon region using the merged rain gauge observations and satellite estimates: Evaluation of monsoon rainfall features. *J. Earth Syst. Sci.*, **116**, 187–198, https://doi.org/10.1007/s12040-007-0019-1.

Sadeghi, M., A. Akbari Asanjan, M. Faridzad, V. Afzali Gorooh, P. Nguyen, K. Hsu, S. Sorooshian, and D. Braithwaite, 2019: Evaluation of PERSIANN-CDR constructed using GPCP V2.2 and V2.3 and a comparison with TRMM 3B42 V7 and CPC unified gauge-based analysis in global scale. *Remote Sens.*, **11**, 2755, https://doi.org/10.3390/rs11232755.

Scofield, R. A., and R. J. Kuligowski, 2003: Status and outlook of operational satellite precipitation algorithms for extreme-precipitation events. *Wea. Forecasting*, **18**, 1037–1051, https://doi.org/10.1175/1520-0434(2003)018<1037:SAOOOS>2.0.CO;2.

Sen Roy, S., and R. C. Balling Jr., 2004: Trends in extreme daily precipitation indices in India. *Int. J. Climatol.*, **24**, 457–466, https://doi.org/10.1002/joc.995.

Shepard, D., 1968: A two-dimensional interpolation function for irregularly spaced data. *Proc. 1968 23rd ACM National Conf.*, New York, NY, ACM, 517–524, https://doi.org/10.1145/800186.810616.

Singh, A. K., V. Singh, K. K. Singh, J. N. Tripathi, A. Kumar, A. K. Soni, M. Sateesh, and C. Khadke, 2018: A case study: Heavy rainfall event comparison between daily satellite rainfall estimation products with IMD gridded rainfall over peninsular India during 2015 winter monsoon. *J. Indian Soc. Remote Sens.*, **46**, 927–935, https://doi.org/10.1007/s12524-018-0751-9.

Singh, R. B., and S. Mal, 2014: Trends and variability of monsoon and other rainfall seasons in Western Himalaya, India. *Atmos. Sci. Lett.*, **15**, 218–226, https://doi.org/10.1002/asl2.494.

Toté, C., D. Patricio, H. Boogaard, R. Van der Wijngaart, E. Tarnavsky, and C. Funk, 2015: Evaluation of satellite rainfall estimates for drought and flood monitoring in Mozambique. *Remote Sens.*, **7**, 1758–1776, https://doi.org/10.3390/rs70201758.

Wilks, D. S., 2006: *Statistical Methods in the Atmospheric Sciences*. 2nd ed. International Geophysics Series, Vol. 100, Academic Press, 648 pp.